1996

Solid-State Sensors, Actuators, and Microsystems Workshop

Late News Poster Session Supplemental Digest

Table of Contents

Author Index

Copyright

1996
Solid-State Sensors, Actuators, and Microsystems Workshop

Hilton Head Island, South Carolina • June 2 - 6, 1996

If you have questions regarding the installation, please contact:

The Printing House
Phone: +1-608-873-4500
Hours: Monday through Friday, 8 am - 5 pm CST
E-mail: graphics@printinghouseinc.com

1996 Solid-State Sensor and Actuator Workshop
June 3 - 6, 1996
Crowne Plaza Resort, Hilton Head Island, South Carolina

LATE-NEWS POSTER SESSION
Wednesday, June 5, 6:30 - 8:00 pm

TABLE OF CONTENTS

TECHNICAL PAPERS

Solid-State Sensors, Actuators, and Microsystems
Workshop

1996
Hilton Head Island, South Carolina
June 2 - 6

PULL-IN DYNAMICS OF ELECTROSTATICALLY-ACTUATED BEAMS

Raj K. Gupta, Elmer S. Hung, Yao-Joe Yang, G. K. Ananthasuresh and Stephen D. Senturia
Microsystems Technologies Laboratories, M.I.T.
Cambridge, MA 02139

ABSTRACT

We report the experimental measurement and simulation of the transient electrostatic pull-in characteristics of micro-structural beams fabricated with silicon surface micromachining. Pull-in dynamics are investigated under the influence of compressible squeezed-film damping (CSQFD) for large amplitude motion. A linearized one-dimensional model, using a fitted damping constant, and a two-dimensional finite-difference model, based on the compressible isothermal Reynold's equation, are used to simulate the experimental data.

INTRODUCTION

Elastically supported microstructures become unstable under a nonlinear electrostatic force beyond an applied voltage called the pull-in voltage. In mechanically static situations, this voltage is termed the static pull-in voltage (V_{PI}). Models for V_{PI} have been used for extraction of material properties and for process monitoring from microelectromechanical system (MEMS) test structures. [1-4]

In mechanically dynamic situations, MEMS devices over small air gaps are subject to CSQFD. This effect has been simulated for large amplitude motion by Yang and Senturia using the nonlinearized form of the compressible isothermal Reynold's equation. [5] Here we investigate the coupled elastoinechanical-electrostatic-CSQFD problem for the large dynamic motion of microstructural fixed-fixed beams by measuring their pull-in times after step voltage applications.

EXPERIMENTS AND SIMULATIONS

Two fixed-fixed polysilicon beams, 610 μm long and 710 μm long, 2.12 μm thick and 40 μm wide over a 2.07 μm gap are placed in a circuit similar to that in Figure 1. [6] A zero-to-peak step input voltage is applied between the beam and a fixed bottom conductor. Similar to that shown in Figure 2, the pull-in time is measured as the delay between the application of the step input and the sharp increase in V_{out} after the beam makes contact to the conductor.
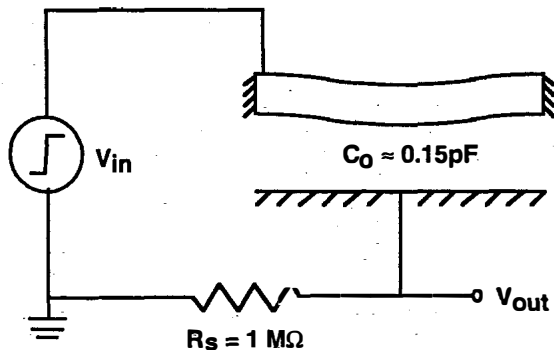
Fig. 1: Circuit used for measuring pull-in times.
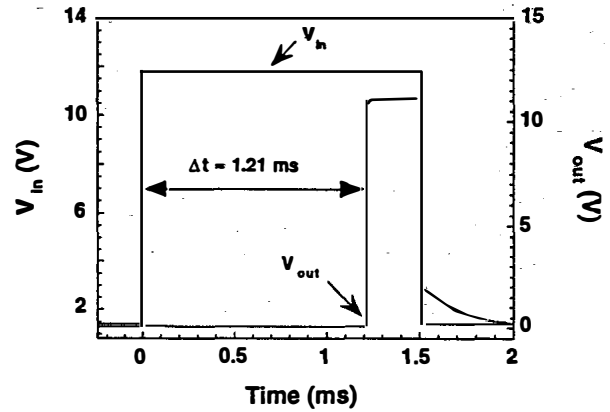
Fig. 2: Oscilloscope data showing Δt, which measures the pull-in time from a static deflection near 1.3 V to pull-in after application of 11.8 V.

Two approaches were taken to model the pull-in time. The first uses a lumped mechanical circuit-equivalent (1D macro-model), similar to the distributed models in [7] for analyzing small amplitude motion of accelerometers. Our model is shown in Figure 3. The beam is a lumped mass m and moves along the x-coordinate, k is a linearized spring constant and b is a linearized damping factor. The electrostatic force is derived from the voltage across the parallel plate capacitance with a gap $h=(g-x)$, where g is the undeflected gap.
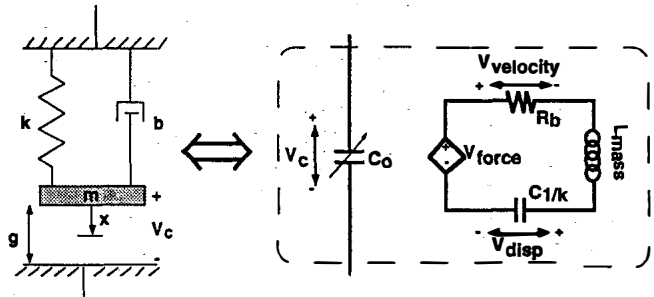
Fig. 3: A mechanical circuit-equivalent of the 1D pull-in macro-model. R_b, L_{mass}, and $C_{1/k}$ have components equal to their MKS subscript values in the base units of Ω, H, and F, respectively. $C_o = \varepsilon_o A / (g - V_{disp})$ and $V_{force} = 1/2 \, \varepsilon_o A V_c^2 / (g - V_{disp})^2 \cdot (1/k)$.

The second approach solves the two-dimensional (2D) finite-difference equation of motion for a uniformly-flat Euler wide-beam (1) coupled to a modified Reynold's equation (2) through a damping pressure P_D [5,8] and to a parallel-plate approximation of the nonlinear electrostatic pressure P_E:

$$\frac{\bar{E} t^3}{12} \nabla^4 h + \sigma_s (h) \nabla^2 h = P_E + P_D - \rho_s \frac{\partial^2 h}{\partial t^2} \quad (1)$$

$$\frac{\partial(hP_D)}{\partial t} = \frac{\nabla \cdot \left(P_D h^3 \nabla P_D \right)}{12 \mu}. \quad (2)$$

The air viscosity μ is 1.82×10^{-5} kg/(m·s). t' is the beam thickness. $\bar{E} = 164$ GPa is the plate modulus and $\sigma_s(h)/t'$ is the gap-dependent stress, where $\sigma_s(h=g)/t' = -3.5$ MPa as determined from the models for V_{PI}. [1] The density of polysilicon, ρ_s/t' is 2200 kg/m^3.

Figures 4 & 5 show the measured and simulated pull-in times for both beams in air. Independent static measurements of V_{PI} for the 610 µm and 710 µm beams indicate they are 8.76 V and 5.54 V, respectively. Both are close to the lowest recorded values for which pull-in times could be measured.
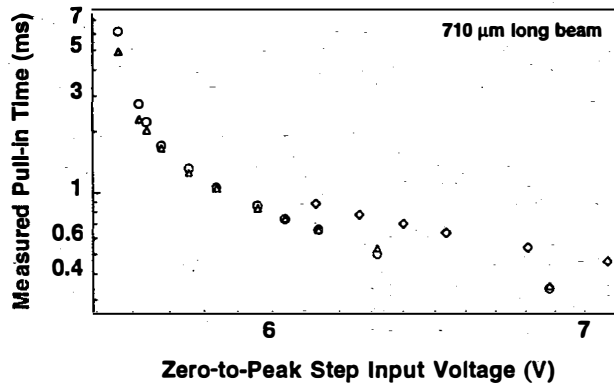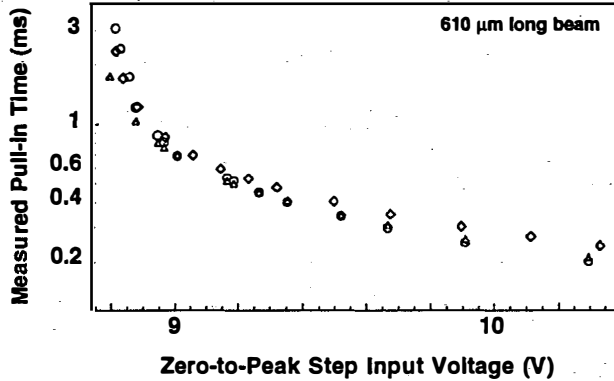
Figs. 4 & 5: Measured pull-in times in air (circles). 1D (triangles) and the 2D (diamonds) simulations are shown for both the 610 µm and 710 µm beams.

For the 1D model, k is chosen by matching the 1D equation for $V_{PI} = (8kg^3/27\varepsilon_oA)^{1/2}$ to the statically measured V_{PI}. With gaps of $g = 2.07$ µm and conductor areas of $A_{610} = 2.44 \times 10^4$ µm^2 and $A_{710} = 2.84 \times 10^4$ µm^2, the 610 µm and 710µm beam have k's equal to 6.33 N/m and 2.94 N/m, respectively. m is determined from the beam geometry and from ρ_s, giving masses of 12 pg and 14 pg, for the two beams. b is determined by finding a best fit to the experimental data using the 1D model. This yields $b = 35 \pm 2$ µg/s for both beams.

In Figure 6, we plot the measured and simulated pull-in times for the 610 µm beam in vacuum at 6×10^{-3} mbar. (Note, 1 atm ≈ 1000 mbar.) The times are an order of magnitude shorter than the air-damped case in Fig 4. Because of inertial effects, the beam can pull in dynamically at voltages below V_{PI}, an effect predicted by the 1D model with $b=0$. When calculated using the k reported above, this dynamic pull-in occurs at 8.04 V, which agrees with the measured pull-in voltage of 8.10 V and the corresponding simulated pull-in voltage of 8.04 V from the 2D model.
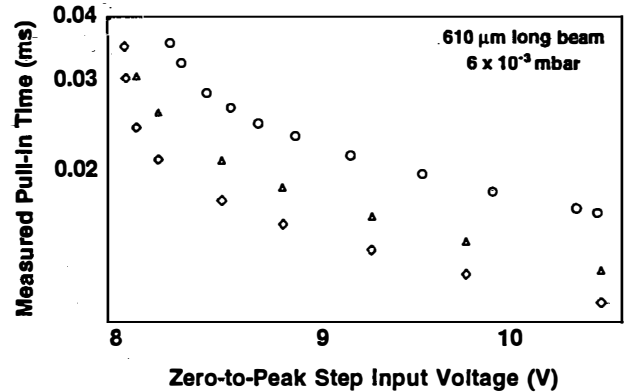
Fig. 6: Measured pull-in times at 6×10^{-3} mbar for the 610 µm beam. Vacuum simulations in 1D (b=0, triangles) including a 40 pF parasitic capacitance on V_{out}, and in 2D ($P_D=0$, diamonds) are also shown.

CONCLUSIONS

We find that the 1D and 2D simulations generally model the pull-in time data from our beams. Additional effects to be included are (1) the breakdown of the continuum flow approximation [9], (2) fringing fields, (3) more precise material constants ($\bar{E}$ and $\sigma_s(h=g)$), and (4) structural damping.

ACKNOWLEDGMENTS

REFERENCES

[1] P. M. Osterberg, et.al., *Solid-State Sensor and Actuator Workshop*, Hilton Head, SC, June 1994, pp. 184-188.

[2] R. Gupta, C. H. Hsu, M. A. Schmidt, and S. D. Senturia, *Transducers 1995 • Volume I*, pp. 269-272.

[3] K. E. Petersen, *IEEE Trans. on Electron Devices*, **ED-25** (1978), pp. 1241-1250.

[4] K. Najafi and K. Suzuki, *MEMS 1989*, Salt Lake City, Feb. 1989, pp. 96-97.

[5] Y. Yang and S. D. Senturia, *Solid-State Sensor and Actuator Workshop*, Hilton Head, SC, June 1996.

[6] MUMPs 5 devices, courtesy of David Koester and Karen Markus of MCNC.

[7] T. Veijola, H. Kuisma, J. Lahdenperä, and T. Ryhänen, *Sensors and Actuators A*, 48 (1995), pp. 239-248.

[8] W. E. Langlois, "Isothermal Squeeze Films", *Quarterly Applied Mathematics*, Vol. XX, No. 2 (1962), pp. 131-150.

[9] E. B. Arkilic, et.al., 1994 ASME: *Application of Microfabrication to Fluid Mechanics*, **FED-Vol. 197**.

COMPLETELY INTEGRATED THERMO-ELECTRO-MECHANICAL ANALYSIS OF MEMS DEVICES

Sandeep Akkaraju, Yie He, Robert Harris, Gene Napadensky, and Fariborz Maseeh
IntelliSense Corporation
16 Upton Drive
Wilmington MA 01887
E-mail: IntelliS@aol.com

ABSTRACT

In this paper we describe the development of a CAD tool for performing completely integrated thermo-electro-mechanical analysis for MEMS devices. As a demonstration of the capability, we analyze the performance of an electrostatic actuator under applied temperature, voltage, residual stress and mechanical loading.

INTRODUCTION

Temperature related issues such as sensitivity, residual stresses and CTE mismatch are important issues in translating MEMS devices into commercial instruments. High temperature processing of micromachined devices such as anodic bonding and doping processes during the fabrication of on-chip electronics can induce significant temperature artifacts in the device performance. Additional process associated effects such as warpage caused by stress gradients in deposited films, process tolerances add to the difficulty of designing MEMS devices. Lack of proper analysis tools have further impeded the successful design and development of micromachined devices and systems.

IntelliSense has been actively involved in developing CAD tools for the MEMS community. We have previously reported the development of a virtual prototyping environment (IntelliCAD™) for designing MEMS [1]. In this paper, we report a key improvement to the IntelliCAD software suite to perform fully integrated thermo-electro-mechanical analysis. The software system allows the user to account for process induced and operating environment effects for the accurate analysis of the real time performance of microdevices.

THEORY

Fully coupled thermo-electro-mechanical analysis is a computationally difficult problem. First, the problem requires mesh compatibility between the electrostatic analysis (usually, boundary element based) engine and the mechanical analysis (usually, finite element or finite difference based) engine. Electrostatic analysis requires the presence of fine mesh around sharp edges or corners where the charge density is concentrated, while the mechanical analysis requires the mesh to be refined near large stress or stress gradient regions.

Second, the discretization grid must track the electrostatically deformed boundaries of the structure--i.e., solve a moving boundary problem. The problem is further complicated by requirements such as automatic or adaptive generation of optimized meshes of structures.

The governing system of equations for a thermo-electromechanical problem can implicitly be expressed as:

$$S = F_m [X_0(T, M), F_e(S + X_0, V)] \qquad (1)$$

where: $X_0(T,M)$ is a vector representing the released structure, S is the discretized structure surface displacement, T is the applied thermal boundary, M is the multi-material property information and V is the applied voltage information. F_e represents the electrostatic force derived from solving the Laplace equation. The final displacement, S, can be obtained by solving the force-displacement equation.

IMPLEMENTATION

The central algorithm for solving coupled thermo-electromechanical problems is described below. First, the IntelliCAD finite element program is used to perform true 3D thermal analysis to determine the temperature distribution, this is followed by the calculation of thermal stress gradients and process induced effects to simulate the released device structure. In the next step, the voltage loads are applied and the electrostatic pressure distribution is calculated using the IntelliCAD 3D electrostatic module. The electrostatic pressure loads are then applied in the finite element mechanical engine and the deformations are recalculated. This procedure is repeated until a preset convergence criterion is reached. This method will converge if:

$$\left| \frac{\partial F_m}{\partial F_e} \cdot \frac{\partial F_e}{\partial S} \right| < 1 \qquad (2)$$

In case of divergence due to electrostatic instability such as pull-in of structures the analysis is terminated.

EXAMPLE

In order to demonstrate the coupled analysis we analyzed a surface micro-machined linear resonating actuator fabricated using the MCNC-MUMPS process [2]. The mask-set (6 masks) used for the device fabrication was obtained from the MCNC MEMS web-page [3].

Figure 1 shows the IntelliCAD solid model of the surface micromachined device (the vertical scale has been exaggerated for the purpose of clarity). The solid model shows the presence of anchors, dimples and the poly interconnect features (*poly0, dimple, anchor1, poly1, poly1_poly2_via, hole1, etc.*).

For the purpose of demonstration, we assumed that the substrate is heated while the resonator is maintained at room temperature. A potential difference of 20 V was applied between the fixed comb and the actuator. We also accounted for the presence of process induced stresses in the deposition of the polysilicon and subsequent doping [4].

RESULTS AND CONCLUSIONS

Figure 2 shows the deformation of the device due to the process induced stresses, operating temperature effects and applied voltage loads - the result of the fully coupled thermo-electro-mechanical analysis. Figure 3 shows a close-up of deformed structure, the warpage induced effects are clearly visible.

The fully coupled analysis has been successfully implemented using the IntelliCAD architecture. The module can successfully handle multi-dielectric effects. The IntelliCAD system seamlessly integrates MEMS process design, device mask layout and fully coupled thermo-electro-mechanical analysis of micromachined devices. The efficacy of the IntelliCAD system has been tested in designing a wide range of micromachined sensors and transducers. This includes -- micromachined pressure transducers, microphones and resonating gyro elements.
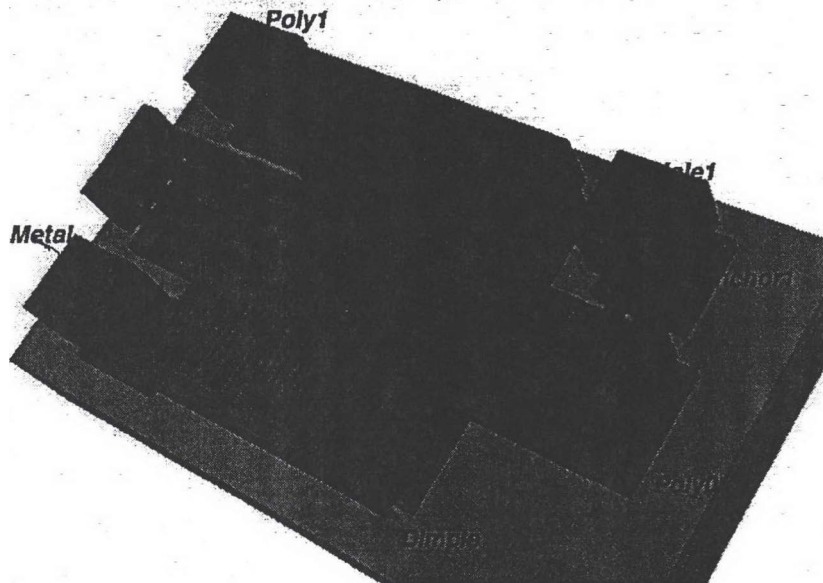
Figure 1. Solid model of a surface micromicromachined linear actuator generated by IntelliCAD using a mask set provided by MCNC.
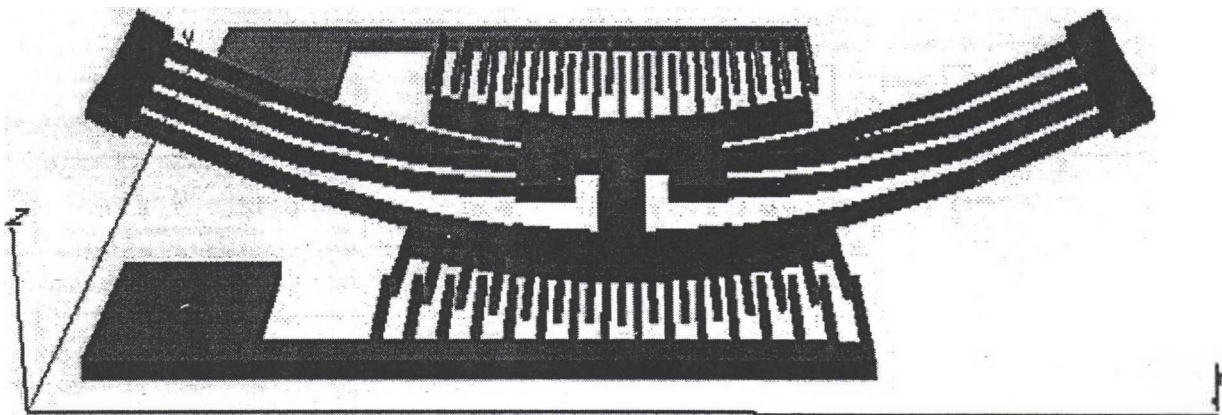
Figure 2. Warpage of the polysilicon structure due to process related residual stresses, thermal loading effects and voltage loads. The finite element analysis was performed using 1169, 20 noded iso parametiic brick elements. The deformation of the structure has been exaggerated for the purpose of clarity.
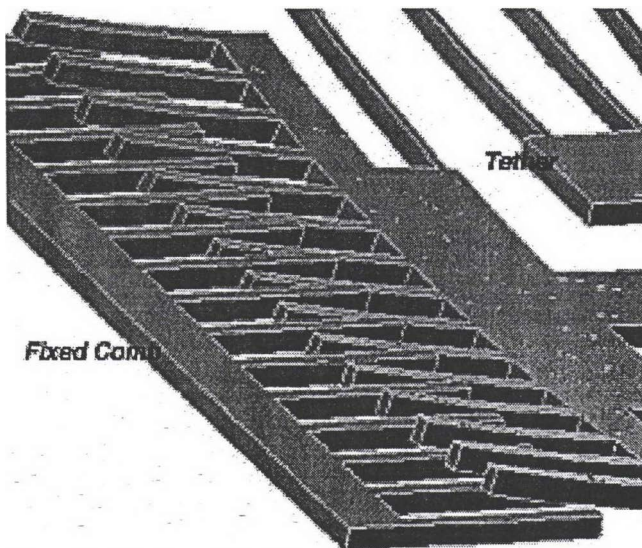
Figure 3. Close-up of the deformation of the comb-teeth. (Deformation has been exaggerated for the purpose of clarity)

ACKNOWLEDGEMENT

REFERENCES

1. Y. He, R. Harris, G. Napadensky and F. Maseeh, "A virtual prototype manufacturing software system for MEMS", *Proceedings of IEEE MEMS '96* (1996)

2. K. W. Markus and D. A. Koester, "Multi-User MEMS Process (MUMPS) - Introduction and Design Rules", Published by *MCNC, Electronics Technologies Division* (1995)

3. Nonparametrized Microelectromechanical Library, *http://mems.mcnc.org/cug/mc5.html* also see the MCNC -MEMS Internet homepage, *http://mems.mcnc.org/mumps/* (1996)

4. IntelliSense Corporation, *MEMaterial® - Solid state thin film database* - Properties of thinfilm polysilicon (1993-1996)

REDUCED LINEARITY ERROR DESIGNS FOR CAPACITIVE MICROMACHINED SENSORS

Christoph Menzel
Ford Microelectronics, Inc.
Colorado Springs, Colorado 80921-3698

ABSTRACT

This paper describes a general design solution which breaks the link between sensitivity (percent deflection) and DC linearity error for a torsional spring, capacitive, micromachined accelerometer. Modeling and device data for a specific sensor configuration show the effectiveness of the design change. The reduced linearity error is achieved by designing in non-linearity that counter balances the device's inherent non-linearity. As the solution involves changing only the relative size of stationary metal electrodes, it has little or no impact on other device functions such as DC and AC response and general device robustness.

INTRODUCTION

The design solution presented herein has found applicability on the transducer of accelerometers used within automotive airbag systems. While automotive linearity requirements are not particularly stringent (~1% of full scale), the high volume production and 6σ goals of automotive manufacturing are in themselves forces for tight tolerances. The transducer is an iteration of a centrally tethered, two beam, capacitive device introduced by Silicon Designs[1]. The heavy/light mass ratio is approximately 3:1. Differential capacitors are formed by independent, stationary metal electrodes underneath the heavy and light sides of the single crystal silicon structure.

The interface electrical circuit outputs a delta-sigma pulse stream [2,3] proportional to $\Gamma = (C_h - C_l) / (C_h + C_l)$ where C_h and C_l are the heavy and light side capacitance values respectively.. Switching voltage levels applied to the stationary electrodes transfer charge on-to(off-of) the heavy(light) sides of the element. The charge flow is analyzed by a first order "charge mode" delta-sigma modulator[2]. The output frequency is proportional to the total amount of charge transferred, which in turn is dependent, through the capacitance, on the deflection of the plate caused by acceleration. The voltage transitions are set using EEPROM and hence, by setting the magnitude of the transitions, the product can be fully calibrated for zero-g output and gain.

The sensor system is an open loop system. Maximum deflections and electrical gain parameters are designed to function in the 10% deflection range at 50g full scale. In addition, the system architecture requires that the transducer provide mechanical filtering in the 400 Hz range.

SOURCES OF NON-LINEARITY

The sources of non-linearity in a differential torsional capacitive system can be listed. The primary contributors are:
- Large deflections i.e. deviations form Hooke's law resulting only from the size of the deflection.
- The non-linear nature of $\partial Cap/\partial gap$ within a system where $\partial gap/\partial accel$ is linear.
- Common Mode Signals.
- "Extra," systematic forces e.g. sensing voltage forces.

Of this list, the first item will not be considered. The effect of these sources on Γ are investigated below. Other potential sensor outputs are ∂C, and $C_h - C_l$. These outputs are significantly more non-linear than gamma [2] and will not be investigated here.

NON-LINEAR NATURE OF $\partial CAP / \partial GAP$

In general the resultant change in capacitance is not linear for linear changes in gap. As such, using either ∂C, or $C_h - C_l$ yields rather non-liner outputs. By contrast, using Γ yields a remarkably linear sensor. In terms of differential and common mode gap displacements, Ddm and Dcm respectively, the first few terms of a series expansion for Γ gives:

$$\Gamma = \frac{(-\frac{Ddm}{do} + 2*\frac{Dcm*Ddm}{do^2} - 3*\frac{Dcm^2*Ddm + Ddm^3}{do^3} \ldots)}{(1 - \frac{Dcm}{do} + \frac{Dcm^2 + Ddm^2}{do^2} - \frac{Dcm^3 + 3*Dcm*Ddm^2}{do^3} \ldots)} \quad (1).$$

Here a linear system has been analyzed instead of the torsional system in order to simplify the calculation. The increased linearity of Γ arises from the fact that both the numerator and the denominator have non-linear terms with respect to differential displacement. The two effects tend to cancel each other out.

If no other sources of non-linearity existed, going to a Γ based design would neutralize the inherent non-linearity of $\partial Cap/\partial gap$ sufficiently for virtually every application.

COMMON MODE SIGNALS

Γ is, however, susceptible to common mode signals. Here common mode signal refers to any displacement that causes same direction changes in both the heavy and the light side capacitors. Examples are beam sag or plate curling. From equation 1 it is clear that common mode deflections effect the denominator significantly more than the numerator. Consequently, Γ is effected. If the common mode deflection decreases the gap, then the output is depressed. If the gap is increased, then the output is inflated.

"EXTRA", SYSTEMATIC FORCES

By definition, a voltage must be applied across the capacitor to get capacitive transduction. Hence a force is applied across the plates. Unless the sensing voltage is scaled to compensate for the deflection caused by acceleration, this systematic force will increase at increased deflection. Furthermore, the rate of increase of this force also increases. Theta will no longer be linear with respect to accelerations. Figure 1 shows modeling results of the incremental effect of sensing voltage on a Γ based system.

DESIGN SOLUTION

One approach to designing a reduced linearity error device is to minimize the contribution of each of the sources. With this

approach, the design is pushed towards an insensitive device to reduce the sensing voltage contribution to non-linear. Furthermore, the device needs thick beams to reduce the common mode to differential mode deflection ratio. This approach can cause conflicts with AC response and signal to noise ratio specifications. In addition, it places constraints on device size and processing.
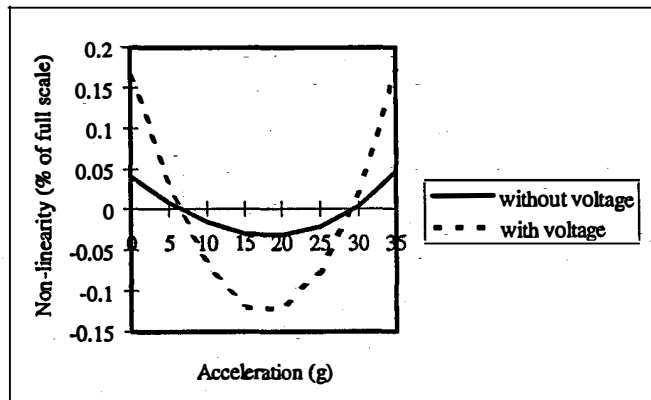
Figure1. Effect of Sensing Voltage on Device Non-Linearity.

A less restrictive, more system oriented approach involves making the heavy side capacitor larger than the light side capacitor. This change makes *Dcm* non-zero even if no common mode displacement occurs. Now, as the element deflects, the denominator gets bigger and works with the common mode deflection to offset the non-linearity caused by the sensing voltage.

In practice, making the heavy side stationary metal plate a different area than the light side stationary metal achieves any arbitrary mismatch ratio. No change in the element structure is required. So AC response, robustness and fabrication processes are not changed. Furthermore, the DC response of the device is not reduced and signal to noise ratio need not be compromised.

MODELING RESULTS

Modeling confirmed that the design change would, in fact, reduce the linearity error. In addition, is showed approximately what level of mismatch was needed given the design's inherent common mode deflections and that no other device outputs were significantly effected. Modeling was done using a Ford Microelectronics Inc. proprietary computer model that converts geometry into a mass/spring system, performs the device calibration process and then "tests" the device at various accelerations. All calculations included sensing voltage effects.

Results are shown in Figure 2. The only device parameters that changed in any significant manor were the linearity error and the calibration value that controls zero-g output. The change in linearity error is reasonably linear with respect to mismatch ratio over the range tested.

EXPERIMENTAL RESULTS

Devices were fabricated using the standard process at 4 levels of mismatch ratio: 1, 1.175, 1.253 and 1.343. Results are shown in Figure 3. The improvements in maximum linearity error are evident and consistent with the modeling and conceptual results.

Regression analysis gives the result:

$$Max. \; L\text{-}error = -.599 * (Mismatch \; ratio) + 1.0354 \; (2)$$

with *adjRsquare= .84*. Equation 2 is not a general equation. Clearly, the intercept term contains information about the device deflection sensitivity and common mode deflection

CONCLUSIONS

In a Γ based system linearity error, deflection sensitivity and sensing voltage relationships can be favorably altered by changing the relative sizes of the stationary metal electrodes. This decoupling gives greater design freedom in setting other device functional parameters. The design advantage is based on an approach that seeks to optimize total device function as opposed to an approach that seeks to optimize components of the total device
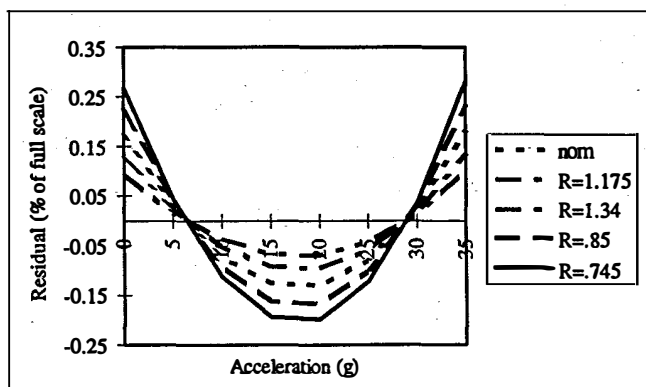
Figure 2. Linearity Error for various designs of mismatch ratio ranging from 1.75 to .745
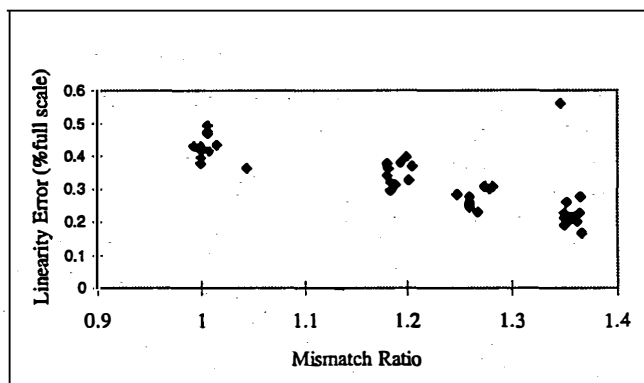
Figure 3. Experimental results of four different levels of mismatch ratio. Maximum linearity error over the zero to 35 g range is used as a measure of the device linearity error.

REFERENCES

1. John Cole, "A New Sense Element Technology for Accelerometer Subsystems", *Transducers '91*, June 24-27, 1991, pp. 93-96.
2. Christopher J. Kemp, Leland "Chip" Spangler, "An Accelerometer Interface Circuit", *IEEE Custom Integrated Circuits Conference Digest 1995*, pp. 345-348.
3. Leland "Chip" Spangler, Christopher J. Kemp, "ISAAC-- Integrated Silicon Automotive Accelerometer", (Unpublished-to be published in *Sensors and Actuators 1996*)

HIGH-FIDELITY CFD SIMULATIONS OF MICROFLUIDIC DEVICES

M.M. Athavale, A.J. Przekwas

CFD Research Corporation, 3325 Triana Blvd., Huntsville, AL   35805

ABSTRACT

Current state-of-the-art Computational Fluid Dynamics (CFD) techniques are applied to two microfluidic devices. Flow simulations in a bistable microfluidic amplifier and a micropump with dynamic valves were performed with CFD-ACE, an advanced CFD code. The bistable amplifier simulations showed good agreement with experiments in steady-state and switching modes and hysteresis behavior. Preliminary simulations of the flow in a micropump with dynamic valves are in progress and flow rectification is correctly predicted. An advanced, integrated, CAD environment for MEMS involving 3D geometry models/meshing, fluids/structures solver and visualization tools is proposed.

INTRODUCTION

Advances in the CFD techniques coupled with the speed and capabilities of the computer hardware has made it possible to use these techniques for complex flow problems with good confidence and fast turnaround times. The work reported here is a demonstration of use of CFD techniques to microfluidic devices. The eventual aim of the present effort is to develop a virtual computational environment (VCE) for multi-disciplinary analyses of microfluidic devices. It will contain virtual model "assembly tools", advanced analysis techniques, graphics driven menus for quick problem set-up and parallel processing capability to provide a powerful tool that can be used in the design and optimization process of microfluidic devices.

CODE DESCRIPTION

The simulations were performed using CFD-ACE, an advanced CFD code developed at CFDRC[1]. This code uses a finite-volume, pressure-based methodology for integration of the Navier-Stokes equations on body-fitted coordinate (BFC) grids. The code has an implicit, structured grid, multi-domain solution capability. The physical and numerical models include high order spatial and temporal discretization, selection of boundary types, turbulence models, and a moving grid algorithm. This code has been validated using a variety of benchmark, and experimental flow problems. Currently it is being applied to microfluidic device simulations.

SIMULATION RESULTS

1. Bistable Wall Attachment Amplier

This device was described by Vollmer et.al.[2], and can be used as a fluidic amplifier or as an actuator/switch. A description of the problem and grid used is shown in Figure 1. Working gas at supply pressure P_s is fed to the supply nozzle which forms a jet. Position of this jet is controlled by application of control pressure P_c at one of the control ports. The jet pressure at the output port is used
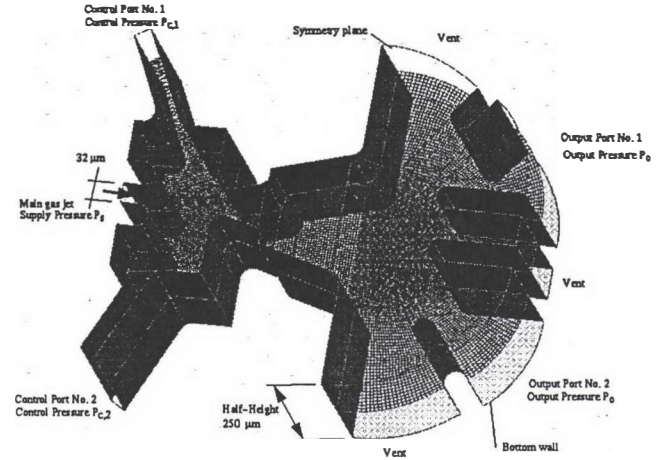
Figure 1. Flow domain, boundary conditions and computational grid for the amplifier.

to actuate or drive other micro-devices. The amplifier shows a hysteresis behavior during switching due to the Coanda effect at the walls as shown in Figure 2, where pressure P_o at the output port opposite to the control port is plotted as a function of P_c in the increasing and decreasing mode.
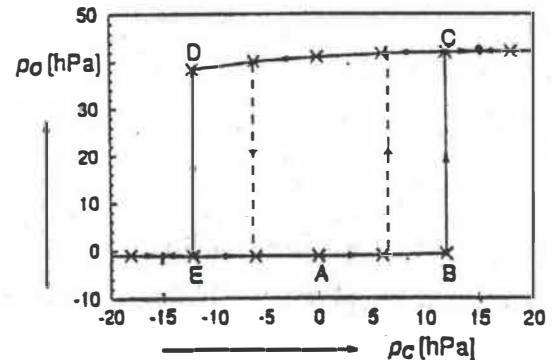
Figure 2. Swiching behavior of Bistable amplifier [2]. The dashed lines indicate the predicted switching behavior.

Simulation were performed to a) predict the steady-state jet at stable positions and calculate the output jet pressures, and b) vary P_c in the hysteresis region to see if the observed hysteresis behavior is predicted. Both items are needed to give a successful demonstration result.

1.1 Problem Description : An 18-domain, 2-D, BFC structured grid, with 15K cells was generated; the grid and boundary conditions are shown in Figure 1. The jet width was set at 32 microns. Nitrogen gas was the working fluid with density=1.15 kg/m^3 and dynamic viscosity=17.8 mPa-s. The supply pressure P_s was 33 hPa(gage). The control pressure P_c was applied at control port No. 2 (Figure 1), and all other ports were kept at 0 Pa (gage). The flow was assumed

to be laminar and with constant fluid properties.

1.2 Results of Simulations : Steady state jet results in terms of the horizontal velocities are shown in Figures 3a and 3b where the P_c was set to +/- 15 hPa to generate stable jets. The simulations used quiescent flow initial conditions. Comparison with Figure 2 shows that the jet positions are consistent with the experimental data. The maximum calculated jet pressure P_o at the output port is 75 hPa, which compares with an experimental passage-average value of 40 hPa. Two series of steady-state runs were performed next to simulate the switching behavior and hysteresis loop (Figure 2). These runs consisted of (a) series A where starting from the solution for $P_c = 15$ hPa, the control pressure was decreased to -12 hPa, and (b) series B where P_c=-15 hPa at start and was increased to +12 hPa. In both cases, the converged solution at the previous higher/lower P_c setting was used as the initial condition for the next run. Results of the series A are shown in Figures 4a through 4d. The jet starts out exiting in output port No. 1 for P_c =15 hPa, and is seen to stay in that position till P_c is dropped to -6 hPa; further lowering of P_c then moves the jet from the upper to lower output port. A symmetrical trend was seen in the series B runs (results not shown) where P_c was increased from -15 hPa to 12 hPa. The predicted switching pressures are between +/- 6 hPa and -/+ 12 hPa which compare with P_c values of +/- 12 hPa seen in Figure 2. Time-dependent simulations of the switching sequence also showed similar behavior.

2. Micropump Simulations

One class of micropumps use dynamic valves with diffuser shaped inlet/exit channels to provide a net fluid motion from inlet to exit. One such geometry was described by Gerlach and Wurmus [3] with high diffuser angles, and relies on flow separation in the diffusing direction to generate flow rectification.

2.1 Problem Description : A 7 mm. square pump chamber with rectangular inlet and outlet sections with 70 degree diffuser section angles was used, with a deforming top wall. A 3-domain grid with 18000 cells was generated and a 'solids model' of the pump is shown in Figure 5.

2.2 Simulation Results : Preliminary time-dependent simulations were carried out at a frequency of 3 KHz. The deformation amplitude is unknown, and needs to be matched with one experimental data point. After this anchoring, additional parametrics can be worked out. A typical velocity plot through the cross-section in the pump is shown in Figure 6, which shows the flow separation in the inlet diffuser during the pumping part of the cycle.

CONCLUSIONS

These simulations demonstrate the ability of CFD-ACE code to treat the complex geometries of the microfluidic devices considered here and provide reasonably accurate results of complex problem of the bistable amplifier. Additional validation problems and demonstration problems including simulations in microvalves are underway to establish the usefulness of the advanced CFD techniques in the analyses and designs of microfluidic devices.

This work was performed under ARPA/ETO SBIR Program and this support is greatly appreciated.

REFERENCES

1. CFD Research Corporation, "CFD-ACE User's Manual", (1994).

2. Vollmer, J., Hein, H., Menz, W., and Walter, F., "Bistable Fluidic Elements in LIGA Technique for Flow Control in Fluidic Microactuators", *Sensors and Actuators A*, (1994), Vol. 43, pp. 330-334.

3. Gerlach, T., and Wurmus, H., "Working Principle and Performance of the Dynamic Micropump", *Sensors and Actuators A*, (1995),Vol.50, pp.135-140.

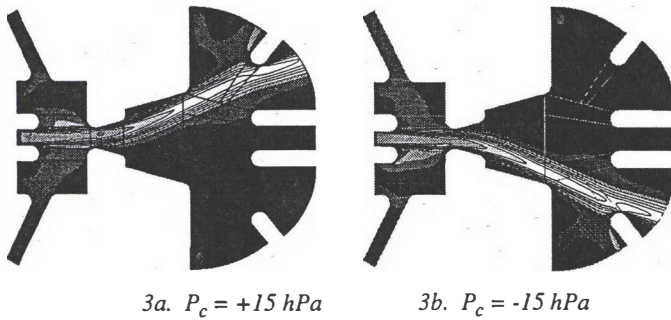3a. $P_c = +15\ hPa$ 3b. $P_c = -15\ hPa$

Figure 3. Steady-State, Stable jet configurations. P_c applied at the lower control port.
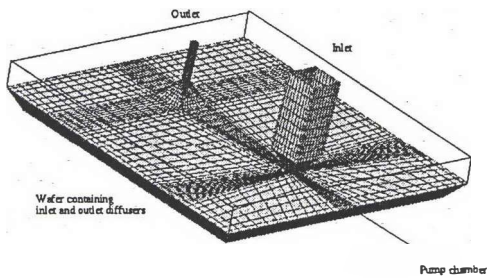
Figure 5. 'Solids model' of the micropump [3].
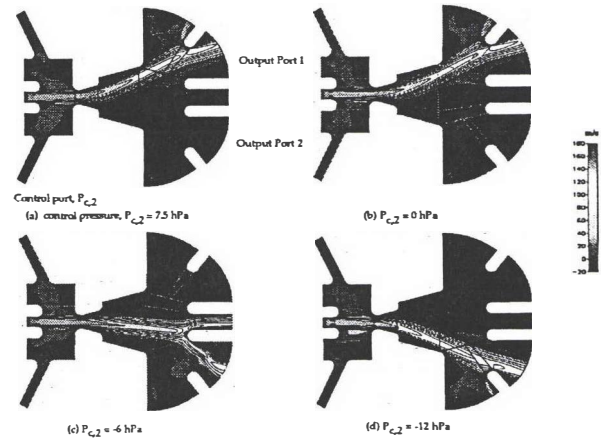

Figure 4. Dynamic Switching behavior of the amplifier, horizontal velocities.
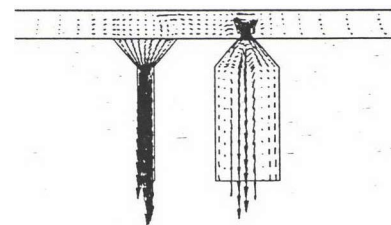

Figure 6. Velocity in pump cross-section during 'down-stroke'.

Biochemical Analysis on a Microchip

Stephen C. Jacobson and J. Michael Ramsey

Chemical and Analytical Sciences Division
Oak Ridge National Laboratory
P.O. Box 2008
Oak Ridge, Tennessee 37831-6142

ABSTRACT

A microchip that performs an automated restriction fragment analysis is demonstrated. The device mixes a DNA sample with a restriction enzyme in a 0.7 nl reaction chamber and after a digestion period injects the fragments onto a 67-mm long capillary electrophoresis channel for sizing. Materials are precisely manipulated under computer control within the channel structure using electrokinetic transport. Digestion of the plasmid pBR322 by the enzyme Hinf I and fragment analysis are completed in 5 min using 30 amol of DNA and 2.8 x 10^{-3} units of enzyme per run.

INTRODUCTION

Important problems in biology and medicine will benefit from the ability to perform automated, rapid, and precise biochemical procedures on minute quantities of material in a highly parallel fashion. There is promise that microfabricated components can be integrated into a single device to solve a complete chemical or biochemical procedures. Simple but powerful examples of integrated devices for performing chemical reactions and separations have been demonstrated using monolithic devices [1-2]. The advantages of integrated devices that perform chemistry and chemical analysis may be quite similar to those realized by the microelectronics industry through the integrated circuit. Potential advantages include low cost, compact devices with high speed processing while improving operational simplicity and reliability and the added benefit of parallel architectures for solving large problems. Moreover, integration of chemical processing and analysis functions allows automated manipulation of samples and reagents at volumes orders of magnitude smaller than is feasible manually or robotically.

Miniaturized devices that have been fabricated primarily involve electrically driven separation techniques including capillary electrophoresis [3-9], synchronized cyclic electrophoresis [10], free-flow electrophoresis [11], open channel electrochromatography [12], and capillary gel electrophoresis [13-15]. Devices that integrate chemical reactions with analysis include capillary electrophoresis with pre- and post-separation derivatization [1, 16]. These devices have exhibited the features mentioned above. Here, we demonstrate a monolithic integrated device for performing a biochemical analysis procedure.

EXPERIMENTAL SECTION

The microchips are fabricated from glass substrates using standard photolithographic, wet chemical etching and bonding techniques as previously described [8]. The microchip design is depicted in Figure 1. The reaction chamber and separation column are 1 and 67 mm long, respectively, having a width at half-depth of 60 µm and a depth of 12 µm; the reaction chamber has a corresponding volume of 0.7 nl. The electroosmotic flow is minimized by the covalent immobilization of linear polyacrylamide.
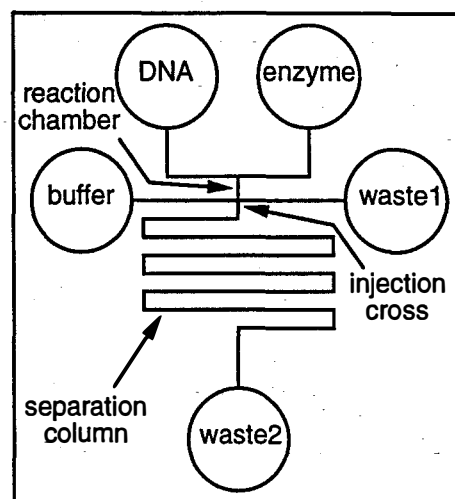
Figure 1. Schematic of a microchip with an integrated pre-column reactor (0.7 nl volume) and 67-mm serpentine separation column.

Chip performance and separations are monitored using laser induced fluorescence (LIF). The reaction buffer is 10 mM Tris-acetate, 10 mM magnesium acetate, and 50 mM potassium acetate. The reaction buffer is placed in the DNA, enzyme and waste 1 reservoirs (Figure 1). The separation buffer is 9 mM Tris-borate with 0.2 mM EDTA and 1% (w/v) hydroxyethyl cellulose. The separation buffer is placed in the buffer and waste 2 reservoirs. The concentrations of the plasmid pBR322 and enzyme Hinf I are 125 ng/µl and 4 units/µl, respectively. The digestions and separations are performed at room temperature (20°C).

RESULTS AND DISCUSSION

First, the DNA and enzyme are electrophoretically migrated into the reaction chamber. A voltage is also applied to the buffer reservoir to prevent the DNA and enzyme from migrating onto the separation column. After the reaction chamber is loaded and is at equilibrium, the digestion can be performed either dynamically with the electric potentials still applied to the chip or statically by removing all electric potentials. To perform the fragment size analysis following digestion, the products are introduced onto the separation

column by applying a potential between the DNA and enzyme reservoirs and the waste 2 reservoir with potentials at the buffer and waste 1 reservoirs removed for a brief period of time, 1 to 10 s. To break off the injection plug and to perform the electrophoretic separation, the potentials at the buffer and waste 1 reservoirs are reapplied.

The fragments are resolved using 1.0% (w/v) hydroxyethyl cellulose as the sieving medium. Figure 2 shows an electropherogram of the restriction fragments of the plasmid pBR322 following a 2 min digestion by the enzyme Hinf I. To enable efficient on-column staining of the double-stranded DNA after digestion but prior to interrogation, the intercalating dye, TOTO-1 (1 µM), is placed in the waste 2 reservoir only and migrates countercurrent to the DNA. As expected, the relative intensity of the bands increases with increasing fragment size because more intercalation sites exist in the larger fragments. The unresolved 220/221-bp and 504/517-bp fragments have higher intensities than adjacent single fragment peaks due to the band overlap.

Figure 2. Electropherogram of products from the digestion of the plasmid pBR322 by the enzyme Hinf I. The separation field strength is 380 V/cm, and the separation length is 67 mm. The numbers correspond to the fragment lengths in base pairs.

The digestion times ranged from 9 to 189 s. The 9-s reaction period corresponds to the transit time of the plasmid through the reaction chamber and is the minimum reaction time. For other reaction times, the voltage to the chip is removed to allow digestion to occur. The intensity of the 1632-bp and 504/517-bp fragment peaks increases for reaction ti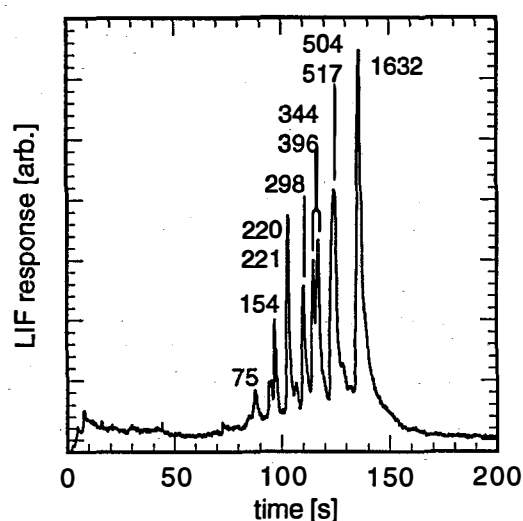mes from 9 s to 129 s (2 min dwell time plus 9 s transit time) by ≈ 10 times, but for a 189 s reaction period (3 min dwell time plus 9 s transit time), no further increase in fragment yield is observed.

ACKNOWLEDGEMENTS

REFERENCES

1. S.C. Jacobson, R. Hergenröder, A.W. Moore, Jr., and J.M. Ramsey, "Precolumn Reactions with Electrophoretic Analysis Integrated on a Microchip," *Anal. Chem.*, 66, 4127 (1994).
2. S.C. Jacobson and J.M. Ramsey, "Integrated Microdeivce for DNA Restriction Fragment Analysis," *Anal. Chem.*, 68, 720 (1994).
3. D.J. Harrison, A. Manz, Z. Fan, H. Lüdi, and H.M. Widmer, "Capillary Electrophoresis and Sample Injection Systems Integrated on a Planar Glass Chip," *Anal. Chem.*, 64, 1926 (1992).
4. A. Manz, D.J. Harrison, E.M.J. Verpoorte, J.C. Fettinger, A. Paulus, H. Lüdi, and H.M. Widmer, "Planar Chips Technology for Miniaturization and Integration of Separation Techniques into Monitoring Systems. Capillary Electrophoresis on a Chip," *J. Chromatogr. 593*, 253 (1992).
5. D.J. Harrison, K. Fluri, K. Seiler, Z. Fan, C.S. Effenhauser, and A. Manz, "Micromachining a Miniaturized Capillary Electrophoresis-Based Chemical Analysis System on a Chip," *Science, 261*, 895 (1993).
6. C.S. Effenhauser, A. Manz, and H.M. Widmer, "Glass Chips for High-Speed Capillary Electrophoresis Separations with Submicrometer Plate Heights," *Anal. Chem.*, 65, 2637, 1993.
7. K. Seiler, D.J. Harrison, and A. Manz, "Planar Glass Chips for Capillary Electrophoresis: Repetitive Sample Injection, Quantitation, and Separation Efficiency," *Anal. Chem., 65*, 1481 (1993).
8. S.C. Jacobson, R. Hergenröder, L.B. Koutny, R.J. Warmack, and J.M. Ramsey, "Effects of Injection Schemes and Column Geometry on the Performance of Microchip Electrophoresis Devices," *Anal. Chem.*, 66, 1107 (1994).
9. S.C. Jacobson, R. Hergenröder, L.B. Koutny, and J.M. Ramsey, "High Speed Separations on a Microchip," *Anal. Chem.*, 66, 1114 (1994).
10. N. Burggraf, A. Manz, C.S. Effenhauser, E. Verpoorte, N.F. de Rooij, and H.M. Widmer, "Synchronized Cyclic Capillary Electrophoresis - A Novel Approach to Ion Separations in Solution," *J. High Res. Chromatogr., 16*, 594 (1993).
11. D.E. Raymond, A. Manz, and H.M. Widmer, "Continuous Sample Pretreatment Using a Free-Flow Electrophoresis Device Integrated onto a Silicon Chip," *Anal. Chem.*, 66, 2858 (1994).
12. S.C. Jacobson, R. Hergenröder, L.B. Koutny, and J.M. Ramsey, "Open Channel Electrochromatography on a Microchip," *Anal. Chem.*, 66, 2369 (1994).
13. C.S. Effenhauser, A. Paulus, A. Manz, and H.M. Widmer, "High-Speed Separation of Antisense Oligonucleotides on a Micromachined Capillary Electrophoresis Device," *Anal. Chem.*, 66, 2949 (1994).
14. A.T. Woolley and R.A. Mathies, "Ultra-High-Speed DNA Fragments Separations Using Microfabricated Capillary Array Electrophoresis Chips," *Proc. Natl. Acad. Sci. USA, 91*, 11348 (1994).
15. A.T. Woolley and R.A. Mathies, "Ultra-High-Speed DNA Fragments Separations Using Microfabricated Capillary Array Electrophoresis Chips," *Anal. Chem.*, 67, 3676 (1995).
16. S.C. Jacobson, L.B. Koutny, R. Hergenröder, A.W. Moore, Jr., and J.M. Ramsey, "Microchip Capillary Electrophoresis with an Integrated Postcolumn Reactor," *Anal. Chem.*, 66, 3472 (1994).

APPLICATION OF SURFACE MICROMACHINING TO EMBRYO LABELING

Lin Wang and David J. Beebe
University of Illinois at Urbana Champaign
Department of Electrical and Computer Engineering
and the Beckman Institute
Urbana, IL 61801

Allen R. Williams and Kim D. Easley
Louisiana Tech University
Department of Animal Science
Ruston, LA 71272

ABSTRACT

Surface micromachining techniques are employed to develop two novel embryo labeling techniques. Polysilicon micro branding irons are fabricated and used to create 30μm × 30μm brands on the zona of bovine embryos. Patterned polysilicon micro tags are fabricated and attached to bovine embryos with agarose gel. Both methods demostrate the potential for batch labeling of biological objects.

INTRODUCTION

Embryo transfer and in vitro fertilization are rapidly growing fields in both animal and human reproduction. Since the first report of in vitro fertilization of in vitro matured bovine follicular oocytes in 1977, the procedures have become widely used [1]. After retrieval from female donors, immature oocytes are matured, fertilized, cultured and finally implanted back into cows. The implanted embryos can worth $300-$1,500 each. It is critical that embryos from each donor be correctly identified through all stages of culture and manipulation. The only method currently available for oocyte/embryo identification is manual labeling of embryo containers. This method is subject to logistical error and contributes to low survivability of embryos. Embryos with unique pedigrees must be cultured separately in order to trace their development. The survival rate of the embryos is consequently reduced as embryos cultured in groups have a significantly higher survival-to-hatching rate versus those cultured separately [2]. Therefore it is important to develop a new method for the oocyte/embryo identification capable of labeling individual embryos. Such a method would enhance survival rate and reduce the chance of mislabeling.

METHODOLOGY

A bovine embryo has a spherical structure, composed of the inner mass cells (yolk) and zona pellucida (zona). The yolk is concentrically surrounded by the zona. The diameter of the bovine embryo is typically 100μm. The zona is a gel-like protein structure, with a thickness of 10-15μm.

ELECTROTHERMAL BRANDING

Electrothermal branding uses electrical energy to increase the temperature of a local region on the embryo surface to the point where molecular destruction or tissue damage occurs. The damaged area, if visible, can be used as a label. The extent of the damage depends on the heat intensity at the iron tip and duration of heat deposition. Control of the heat deposition, particularly in a small well defined region, is an intricate but necessary manipulation to make a label on the region of interest as well as to avoid unnecessary damage to other regions of the embryo. By passing electric current through a miniature patterned polysilicon heating element, a micro branding iron can be realized. By touching the embryo on the hot surface of a branding iron, the pattern of the iron can be burned on the zona surface.

TAG-ATTACHMENT LABELING

Tag-attachment labeling involves adhering a thin (2-4μm), 10μm×10μm to 50μm×50μm patterned polysilicon tag to the surface of the embryo or implanting the tag into the perivitelline space. The unique patterns on the tags serve as the labels. Individual micro tags are suspended over cavities on a substrate via small connecting bars. By breaking or removing the connecting bars, the tags will be released. The released tags can be picked up using micro pipettes via vacuum or electrostatic attraction. Organic glues, such as agarose gel, can be used to adhere the tags to the embryo surfaces.

FABRICATION

The micro branding irons and tags were fabricated via the three-layer polysilicon surface micromachining process of the Multi-User MEMS Process (MUMPs) program at the MEMS Technology Applications Center in North Carolina. Referring to Figure 1, a 500nm thick low stress silicon nitride layer was first deposited on a phosphorous doped n-type (100) silicon wafer as the electrical isolation layer. Next, a 2.0μm PSG (phosphosilicate glass) oxide, a 2.0μm polysilicon, 1.5μm polysilicon, and a 150nm PSG were deposited in sequence as the sacrificial, structure and etch mask layers, respectively. The wafer was then lithographically patterned and RIE etched. Finally, a 0.5μm metal layer was deposited to form the leads for the branding iron and the release mask for the tags. To release the tags a 48% potassium hydroxide (KOH) etchant was used at 85°C for ≈30 minutes. The gold lead material and the PSG layer served as top and bottom masks for the tags. The connecting bars were etched via undercutting. Finally, the tags/irons were released/suspended by removal of the PSG sacrificial layer.
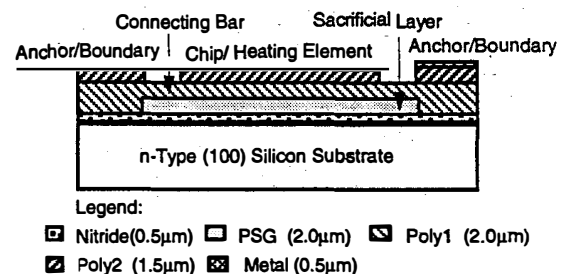

Legend:
- Nitride(0.5μm)
- PSG (2.0μm)
- Poly1 (2.0μm)
- Poly2 (1.5μm)
- Metal (0.5μm)

Figure 1 Side view of micro branding iron or micro tag

RESULTS AND DISCUSSION

ELECTROTHERMAL BRANDING

Hundreds of $30\mu m \times 30\mu m \times 3.5\mu m$ polysilicon branding irons with 27 different shapes were designed and fabricated on a 1cm×1cm silicon die. Figure 2(a) shows a typical micro branding iron array. The irons are connected to the anchor leads and suspended over the substrate. Referring to Figure 2(b), an embryo was held on the tip of a micropipette via vacuum and then touched to the hot surface of a $32\mu m \times 32\mu m \times 3.5\mu m$ serpentine branding iron. Figure 3(a) shows the result. Three burn marks were formed in a region of $\approx 30\mu m \times 30\mu m$ on the zona surface. The linewidth of the brand is $\approx 5\mu m$. The discontinuity of the marks may be a result of the nonplanar embryo surface causing incomplete contact of the iron with the embryo. In addition, there exists a temperature gradient between the positive and negative ends of the iron. The iron region close to the negative lead is cooler and no burn marks formed. Future modifications to the branding iron geometry will allow for a more uniform temperature on the iron surface.
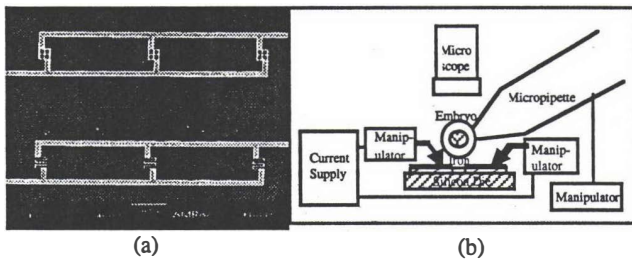

(a)   (b)

Figure 2 (a) SEM of a 2×3 microfabricated array of branding irons (scale bar is 100μm). (b) Experimental setup for polysilicon iron branding (not to scale).

(a)   (b)
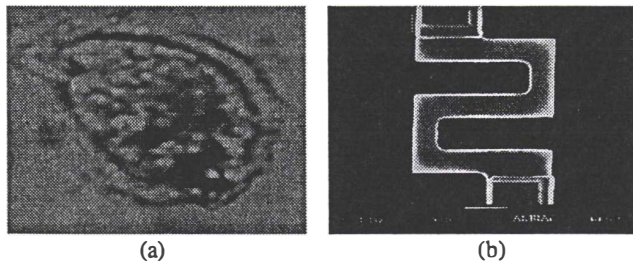
Figure 3 (a)Three burn marks were created in the region of $\approx 30\mu m \times 30\mu m$ on the embryo. The brand corresponds to the branding iron shape. (b) The $32\mu m \times 32\mu m \times 3.5\mu m$ polysilicon iron used for the branding (scale bar is 10μm)

TAG-ATTACHMENT LABELING

Approximately 100,000 polysilicon micro tags with ten unique patterns were fabricated on a 1cm×1cm silicon die. Figure 4 (b) shows the $30\mu m \times 30\mu m \times 3.5\mu m$ micro tags which are suspended by two or four connecting $2\mu m \times 2\mu m \times 1.5\mu m$ bars. After the connecting bars were removed via KOH etching, the tags were picked up and held by a micropipette. The embryos were dipped into agarose gel and placed on a glass slide. By touching the micropipette to the embryos, the tags were released and adhered to the gel coating of the embryo. Figure 4 (a) shows the embryo with "E," and "C" micro tags attached.

Compared with the thermal branding, the tag attachment method is more favorable. However, the security of tag adhesion, compatibility, and viability need to be investigated through the entire embryo culture process.

(a)   (b)
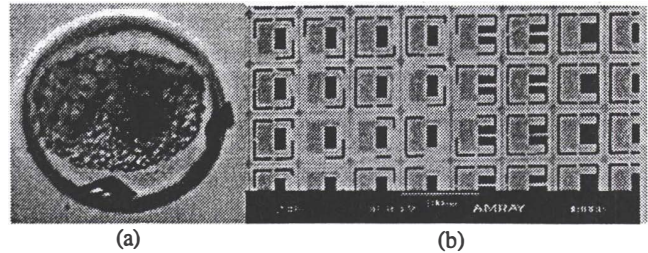
Figure 4 (a) Bovine embryos with attached "E," "C" polysilicon tags (diameter of embryo is 100μm). (b) SEM of microfabricated tags (scale bar is 60μm)

CONCLUSION

The results presented demonstrate that the electrothermal branding and tag-attachment techniques are potentially feasible for embryo labeling. The use of microfabrication techniques is important and has facilitated the development and manufacturing of the micro branding irons and micro tags. The precise control in geometries, sizes, and patterns of the microfabricated polysilicon branding irons and tags allow the labels to be clearly identified. The high consistency and regular micro scale arrangement of the polysilicon irons and micro tags allows the development of batch labeling techniques. Batch labeling systems are being developed to extend the embryo labeling techniques towards practical use. Biocompatibility and embryo viability studies are currently in progress.

ACKNOWLEDGMENTS

REFERENCE

1. A. Iritani and K. Niwa, "Capacitation of bull spermatozoma and fertilization in vitro of cattle follicular oocytes matured in culture," *J. Reprod. Fertilization*, 50: 119-121, (1977).

2. Looney, C. R., B. R. Lindsey, C. L. Gonseth and D. L. Johnson, Commercial aspects of oocyte retrieval and in vitro fertilization (IVF) for embryo production in problem cows, *Theriogenology*, 41: 67-72, (1994).

AN ELECTROCHEMILUMINESCE MICRO-INSTRUMENT

Yun-Tai Hsueh and Rosemary L. Smith
Department of Engineering Electrical And Computer Science, University of California, Davis
Davis, CA 95616

M. Allen Northrup
Microtechnology Center, Lawrence Livermore National Labortory
Livermore, CA

ABSTRACT

This paper describes an electrochemi-luminescence (ECL) instrument, which is micro-fabricated in Silicon and demonstrates its performance. The instrument contains an ECL excitation cell, fluid fill ports and a PIN silicon diode detector. The detection limit at present is tens of atto(10^{-18}) moles of Ru^{+2}(bpy)$_3$.

INTRODUCTION

The ECL microinstrument was designed for DNA quantification after amplification by Polymerase Chain Reaction (PCR). The detection limit is desired to be as low as possible to minimize the amplification and total analysis time. To do so, a high gain, low noise detector such as a photomultiplication tube (PMT), cooled avalanche photodiode, etc., are normally employed. However, our aim is to make a portable instrument, preferably hand-held, therefore size and power requirements exclude those detectors. Here a simple, small, silicon PIN photodiode is used as the detector. This detector could eventually be integrated with the ECL microcell in the same silicon wafer. Our most recent results have demonstrated a detection limit of tens of atto moles of the luminescing label, Ru^{+2}(bpy)$_3$.

THEORY

The chemicals used in this system are tris- N,N' bipyridyl ruthenium (II) (abreviated as TBR) and tripropylamine (TPA). The behavior and related properties of solutions containing these two chemicals have been previously reported [1,2]. To summarize, TPA and TBR are electrochemically oxidized at about the same potential, and became TPA+ and TBR+ respectively. TPA+ is highly unstable and becomes quickly deprotonated. The deprotonated TPA+ (denoted as TPA') is a strong reducing agent, which reduces TBR+ to TBR. During electron transfer, energy transfer also occurs, resulting in photon emission from the excited TBR. This is the underlying principle for ECL. Another possible reaction is that the TPA' also reduces TBR, producing TBR-. When TBR- reacts with TBR+ , light is also emitted [3]. The wavelength of luminescence from TBR is at 630 nm, i.e. orange. In order to use ECL in the quantification of replicated DNA fragments, TBR is attached to a DNA probe which is hybridized in situ with the DNA of interest during PCR. One method for then "collecting" the TBR labeled DNA is to attach the DNA to magnetic beads, which can be then attracted by an external magnet to the oxidizing electrode. This method, which is currently employed by a commercial instrument (Perkin-Elmer

QPCR 5000), has been tested with our micro-instrument, and the preliminary results are presented here.

MICROINSTRUMENT CONFIGURATION

The microinstrument comprises three silicon substrates, which are vertically assembled to form a small cavity with two, thin film Platinum electrodes, V-groove fill ports, and a detector. A silicon, PIN photodiode (EG&G, S1337-66BR), caps off the cavity, with its sensing surface facing the electrodes. The other silicon layers have been anisotropically etched in KOH, coated with Platinum and bonded together, defining the cell volume (150 microliters) and electrode spacing (500 microns). A cross-section of the microinstrument is shown in figure 1. The bottom Pt electrode is where electrochemical oxidation takes place. The upper Pt electrode has a square opening through which ECL can pass to the detector.

A transimpedance pre-amplifier, chopper circuit and lock-in amplifier are connected to the PIN photodiode as shown in figure 2. An EG&G PARC 273 potentiostat is used to apply a triangle voltage waveform to the Pt electrodes for the electrochemical reaction. The output signal, corresponding to the measured light intensity, is monitored and stored on a digital storage oscilloscope and then transfered to a IBM compatible PC for signal processing.

EXPERIMENTAL DETAILS AND RESULTS

Two experiments were conducted to evaluate the instrument. The first experiment used a set of test solutions containing TBR in concentrations of 1nM, 10nM, 100nM and 1μM. Each solution is introduced into the cell with a syringe, followed by measurement, and flushing with water. At a concentration of 1nM, no signal could be distinquished from background noise. However, for 10nM solution, a strong signal can be detected. So the detection limit of this microinstrument configuration for free TBR lies somewhere between 1nM and 10nM. A semilog plot of light intensity vs. concentration is shown in figure 3. The second experiment used TBR labeled magnetic beads, obtained in a test kit from Perkin-Elmer. The kit contains four standards. Standard 1 contains unlabeled magnetic beads, Standard 2 contains magnetic beads bound with 100 attomoles TBR, Standard 3 contains magnetic beads with 1200 attomoles TBR and Standard 4 contains magnetic beads wit 12000 attomoles TBR. Each standard has a solution volume of 40ml. All of the magnetic beads in each standard solution were captured and put into 2 ml of phosphate buffer plus TPA. The beads were re-suspended by shaking and then 150 microliters was removed and introduced into the cell. The same measurement procedures were followed as those used with the unbound TBR, except an external magnet was

Solid-State Sensors, Actuators, and Microsystems Workshop
Hilton Head Island, South Carolina, June 2-6, 1996

used to trap the magnetic beads onto the surface of the bottom Pt electrode. In this manner, quantities of TBR less than 100 attomoles, and in the order of 10 attomoles, were detected. The light intensity vs. time plot for bead standards 2 and 3 is shown in figure 4.

ACKNOWLEDGEMENTS

REFERENCES

1. J. K. Leland and M. J. Powell., J. Electrochem. Soc., 137, pp. 3127-3131 (1990).

2. Y.-T. Hsueh, et. al., 188th Meeting of the Electrochem. Soc., Proceedings of the Symposium on Microstructures and Microfabricated Systems III, pp. 117-122 , (1995).

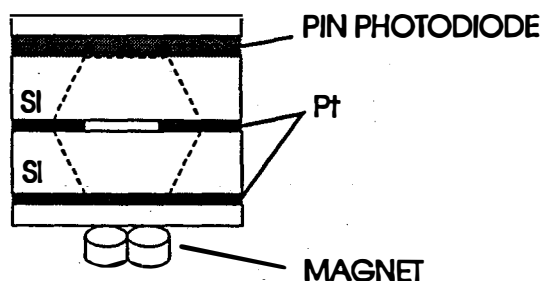3. I. Rubinstein and A. J. Bard, J. Amer. Chem. Soc., 103, 512-516 (1981).

Figure 1. Cross-section schematic of the three silicon layers which form the electrochemical cell, with detector and external magnet.
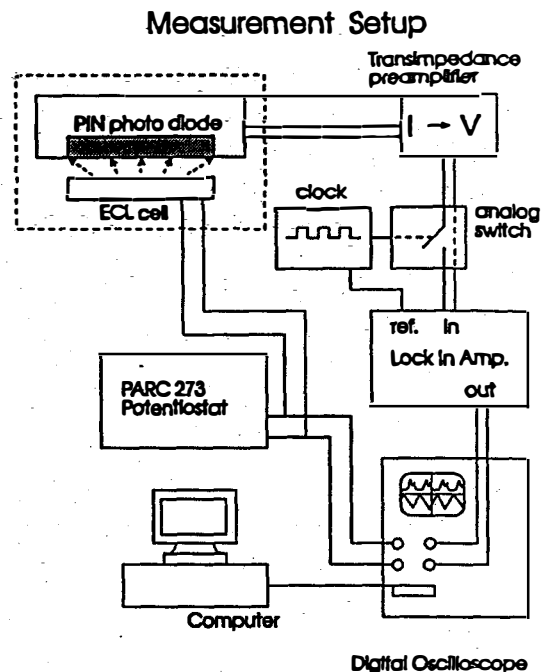

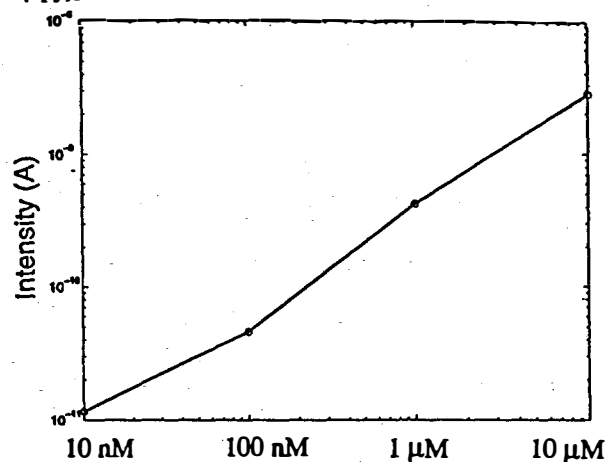Figure 2. Measurement set-up for detection of ECL from $Ru^{+2}(bpy)_3$.
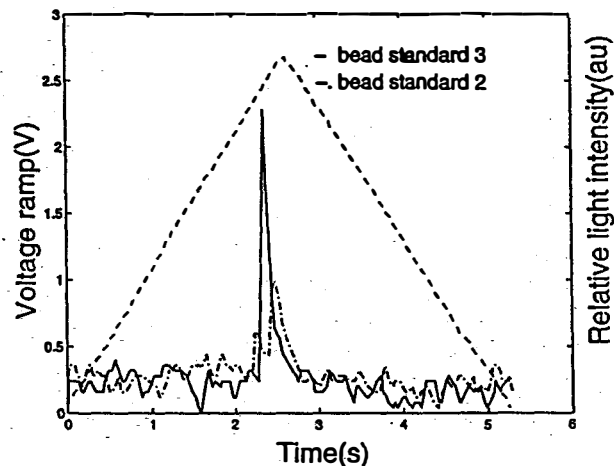

Figure 3. ECL intensity vs.log conc. of TBR.

Figure 4. Pt voltage and photodiode output vs. time for TBR bound to magnetic beads.

BINARY GAS MIXTURE ANALYSIS USING A TWO-DIMENSIONAL ARRAY OF INTERDIGITATED GATE ELECTRODE FIELD-EFFECT TRANSISTORS

John M. Wiseman and Edward S. Kolesar

Texas Christian University, Department of Electrical Engineering
Fort Worth, TX   76129-0001

ABSTRACT

Single component and binary gas mixtures composed of nitrogen dioxide (NO_2) and ammonia (NH_3) were analyzed with a microsensor composed of an array of Interdigitated Gate Electrode Field Effect Transistor (IGEFET) sensor elements coated with copper-, nickel-, and cobalt-phthalocyanine thin films. The design and mode of operation of the IGEFET microsensor facilitated the near-simultaneous measurement of the direct current (DC) and alternating current (AC) electrical response of the metal-substituted phthalocyanine (MPc) thin films upon exposure to the challenge gas mixtures. To facilitate predicting the challenge gas component concentrations for mixtures containing 100-4000 parts-per-billion (ppb) NO_2 and 20-400 parts-per-million (ppm) NH_3, the principal component analysis (PCA) method and multilinear regression technique were applied to the distinctive features identified in the measured response of the IGE structure's DC resistance and the IGEFET transfer function's gain and phase.

INTRODUCTION

The detection and measurement of chemical species, as well as the control of chemical reactions, have widespread applications. Of particular interest with respect to the environment, is the need for small and autonomously operating microsensors that can accomplish the toxic gas monitoring function. Two important classes of environmentally-sensitive compounds include the oxides of nitrogen, especially nitrogen dioxide (NO_2), and ammonia (NH_3).

One type of chemical microsensor technology is the Interdigitated Gate Electrode Field Effect Transistor (IGEFET). As depicted in Figure 1, the IGEFET can be partitioned into two fundamental components: the integrated circuit (IC) and the chemically-sensitive thin film deposited on the surface of the interdigitated gate electrode (IGE) structure of each IGEFET sensing element.
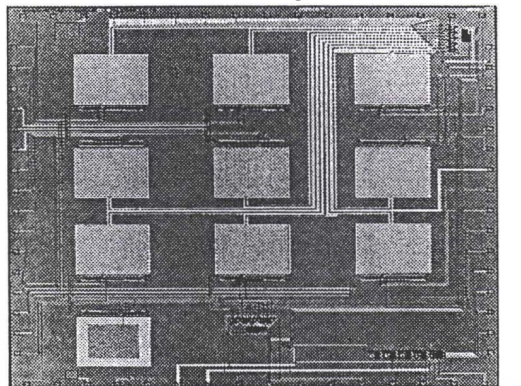

(a)
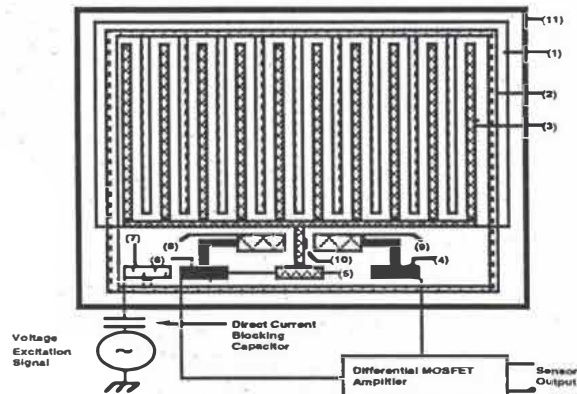
(b)

Figure 1. (a) IGEFET microsensor IC depicting a 3 x 3 two-dimensional array of identical sensors whose independent set of responses can be electrically-multiplexed with the in situ circuitry. (The overall dimensions of the IC are 4466 x 6755 µm. Each IGE structure con-

sists of 34 floating-electrode fingers and 35 driven-electrode fingers. Each finger is 10 µm wide, and the inter-electrode finger spacing is 10 µm. The chemically-active area of the IGE measures 1370 x 1370 µm.) (b) IGEFET physical structure and electrical connections. Legend: (1) copper phthalocyanine (CuPc) thin film, (2) driven-electrode, (3) floating-electrode, (4) MOSFET drain contact, (5) MOSFET gate and floating-electrode contact, (6) MOSFET source contact, (7) driven-electrode contact, (8) MOSFET source, (9) MOSFET drain, (10) MOSFET drain-to-source channel, and (11) host silicon substrate.

EXPERIMENTAL

To facilitate predicting the challenge gas component concentrations for mixtures containing 100-4000 parts-per-billion (ppb) NO_2 and 20-400 parts-per-million (ppm) NH_3, the principal component analysis (PCA) method and multilinear regression [1] technique were applied to the distinctive features identified in the measured response of the IGE structure's DC resistance and the IGEFET transfer function's gain and phase. As depicted in Figure 2 (a)-(c), baseline drift of the IGEFET microsensor was minimized by normalizing the extracted features. The individual challenge gas components (NO_2 and NH_3) were discriminated on the basis of the opposite changes (sign change) they induced in the MPc-coated IGEFET microsensor's electrical properties, the different gas sensitivities revealed by the MPc-films, the time dependence of the electrical changes induced by a challenge gas exposure, and finally, the different gas sensitivities of the frequency-dependent components manifested within the MPc-coated IGEFET transfer function. As depicted in Figure 2 (d)-(f), the predicted challenge gas component concentrations were always within 50% of the known concentrations for all of the gas mixtures analyzed. As anticipated, the smallest error [26% for NO_2, Figure 2 (e) and 14% for NH_3, Figure 2 (f)] was achieved with the single component analysis of each challenge gas using the normalized IGE structure's DC resistance response. The error in the predicted single component analysis of each challenge gas was slightly larger when the analysis was accomplished with the IGEFET transfer function's gain and phase. For the binary gas mixture analysis, the smallest error in the predicted challenge gas concentrations (approximately 25% for each component) was achieved with the IGEFET transfer function's gain response. The phase response was the least effective information for predicting the concentrations of the challenge gas components. As a consequence of the favorable results obtained from the IGEFET transfer function's gain response, a complementary approach was investigated. This technique utilized a lumped-element equivalent circuit model that accurately predicts the variations observed in the IGEFET transfer function's gain and phase Bode plots. When the NO_2 and NH_3 analyses were performed with the conductance parameters extracted from the lumped-element equivalent-circuit model [2], the predicted gas concentration errors were significantly less than the corresponding errors obtained with the gain and phase response feature analyses, and it was never larger than the error predicted when the normalized DC resistance response was used.

(a)

15

(b)

(c)

(d)

(e)

(f)
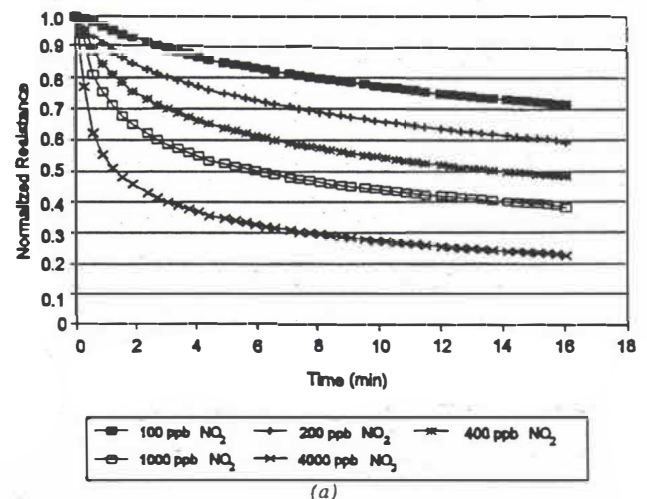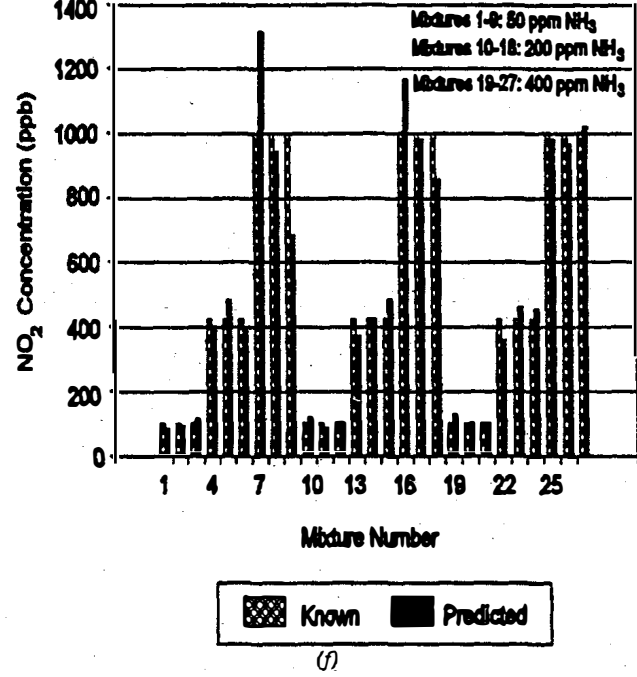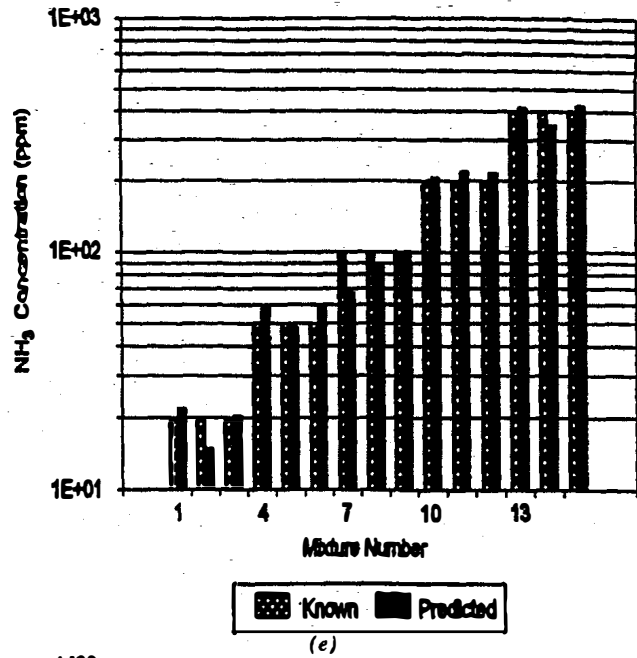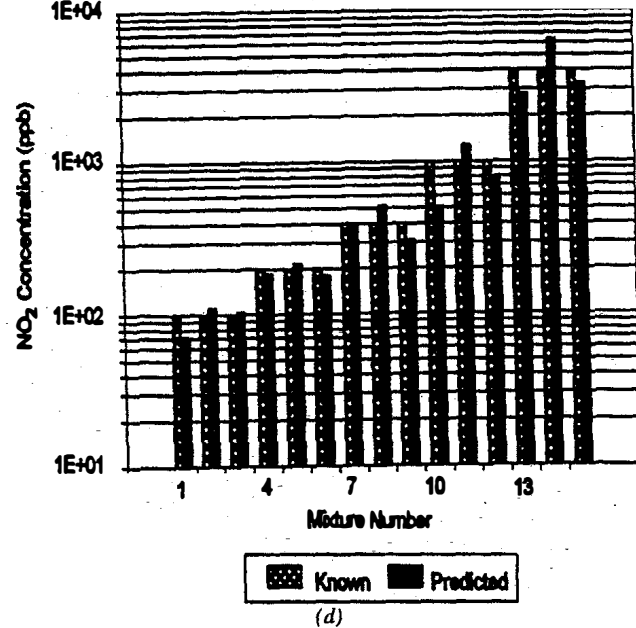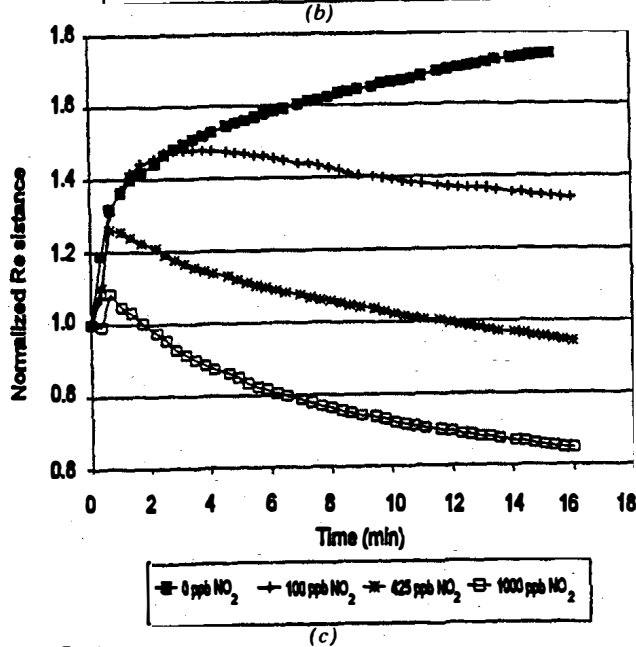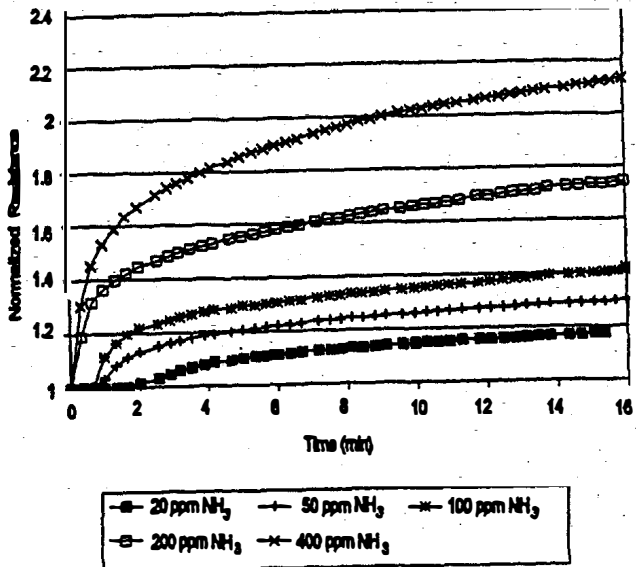
Figure 2. (a) CuPc-coated IGE structure normalized DC resistance response upon exposure to NO_2. (b) CuPc-coated IGE structure normalized DC resistance response upon exposure to NH_3. (c) CuPc-coated IGE structure normalized DC resistance response upon exposure to binary gas mixtures containing 200 ppm NH_3 and various NO_2 concentrations. (d) Comparison of the known (as generated) and predicted NO_2 gas concentrations for 15 different exposures using the normalized DC resistance data. (e) Comparison of the known (as generated) and predicted NH_3 gas concentrations for 15 different exposures using the normalized DC resistance data. (f) Comparison of the known (as generated) and predicted NO_2 gas concentrations for 27 different binary mixture exposures using the normalized DC resistance data. [CuPc film thickness = 0.43 microns; temperature = 100°C].

REFERENCES

1. J. Gardner and P. Bartlett, "Pattern recognition in gas sensing", in *Techniques and Mechanisms in Gas Sensing*, P. Moseley, J. Norris and D. Williams (eds.), Adam Hilger, NY (1991).

2. J. MacDonald, *Impedance Spectroscopy*, John Wiley and Sons, NY (1987).

LOW TEMPERATURE BONDING FOR FABRICATION OF MINIATURIZED CHEMICAL ANALYSIS DEVICES

HongYing Wang, Robert S. Foote, Stephen C. Jacobson and J. Michael Ramsey
Chemical & Analytical Sciences Division, Oak Ridge National Laboratory
P.O. Box 2008, Oak Ridge, TN 37831-6142

ABSTRACT

A low temperature bonding process was developed for the fabrication of microchip devices for liquid phase chemical analysis. Photolithographically etched microchannels on glass substrates were closed by bonding a glass cover plate using sodium silicate as an adhesive. Good channel sealing was achieved at 90 °C for an hour. The performance of the device was evaluated by monitoring the electroosmotic flow on the chip. The strength of the bonding was studied using electrical and mechanical methods. The results were compared with that obtained from the device made from high temperature glass-glass direct bonding.

INTRODUCTION

Microfabricated miniature instruments for complete chemical analysis are receiving increased attention. Various microdevices have been fabricated that perform liquid phase analysis including capillary electrophoresis [1-3], electrochromatography [4], micellar electrokinetic capillary chromatography [5], DNA restriction fragment analysis [6-7], and on-chip chemical reactions with analysis [8]. The devices were fabricated by etching the channel manifolds into glass substrates using standard photolithographic and wet chemical etching methods. The first devices reported used a melting technique to bond the substrate and cover plate at 620 °C to form a network of closed channels [1]. A direct bonding technique was also developed by which the substrate and cover plate were joined and then annealed at 500 °C [3]. However, the high temperature bonding process hindered the further device fabrication, such as immobilizing biological species in the channel, or integration of structural features (e.g. electrodes, waveguides etc.) into the channel. A low temperature bonding process has been reported to bond silicon wafers at 200-300 °C using sodium silicate as a bonding layer [9]. Here, we report a modified process to perform glass-glass bonding using sodium silicate at the process temperature lower than 100 °C.

EXPERIMENTAL

Standard 50 mm x 25 mm glass microscope slide and 22 mm circular or 25 mm x 25 mm square coverslip were used for the bonding experiments. The substrate and the coverslip were treated as follows: (i) Hydrolyze in $NH_4OH/H_2O_2/H_2O$ (2:1:3) solution at 60 °C for 20 min. (ii) Spin-on a dilute solution of sodium silicate in water on the coverslip at 4000 rpm for 10 seconds. (iii) Immediately bring the coverslip in contact with the glass substrate. (iv) Anneal the sample at 90 °C for 1 hour.

The electroosmotic flow was studied on the chip using Rhodamine B as a probe and laser induced fluorescence. The schematic for the measurement of electrical breakdown of the bonding is shown in Fig.1 with a separation of 150 μm between the two channels. The specimens for the mechanical strength measurement were prepared by etching a glass slide to form a
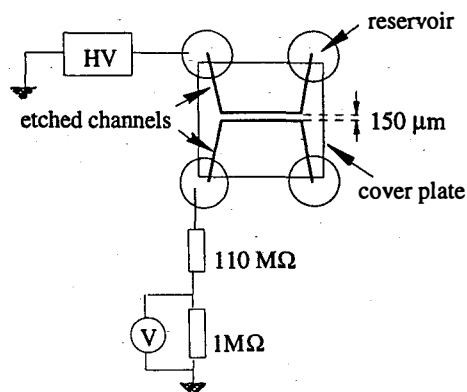
Figure 1. Schematic for the measurement of dielectric strength between microfabricated channels.

triangular area 4 μm above the glass surface and bonding another piece of glass slide on the triangular area. The measurements were done on an Instron 4501 machine and the surface energy was obtained by integrating the area under the load vs. displacement curves [10].

RESULTS AND DISCUSSION

The electroosmotic flow measurements with the chip made using the low temperature bonding method are shown in Fig.2. The measurements were done after flushing the chip with water or 1N NaOH. The NaOH flush regenerates the hydrophilic glass surface and enhances the electroosmotic flow. The results compare well with that obtained from chips made using the high temperature direct bonding method.

Figure 3 shows the electrical breakdown data for the chip
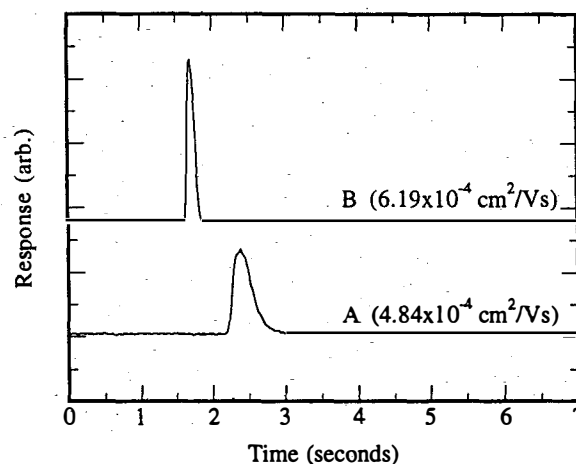
Figure 2. Electroosmotic flow for chips made using the low temperature bonding method: (A) flush with water for 20 mins, (B) flush with 1N NaOH for 20 mins.

bonded with 2 wt.% sodium silicate. The data was used to determine the dielectric strength of the bonding layer. The breakdown occurred at the applied voltage of 6 kV, which corresponds to a dielectric strength of 400 kV/cm. The breakdown was irreversible since a current path was formed after the breakdown, which is believed to be due to the sodium ions in the sodium silicate bonding layer. Compared with the low temperature bonding, the high temperature direct bonding is much stronger with a dielectric strength of 1100 kV/cm, as shown in Fig.4. The breakdown was reversible, as can be seen in Fig.4 in that it "healed" after the applied voltage was reduced. This may be attributed to the fact that the breakdown was caused by the movement of the electrons relative to their nuclei to constitute a displacement current [11]. Therefore the breakdown current of the high temperature bonding is much lower than that of the low temperature bonding.

Figure 3. Electrical breakdown measurement of the chip made using the low temperature bonding method.

Figure 4. Electrical breakdown measurement of the chip made using the high temperature direct bonding method.
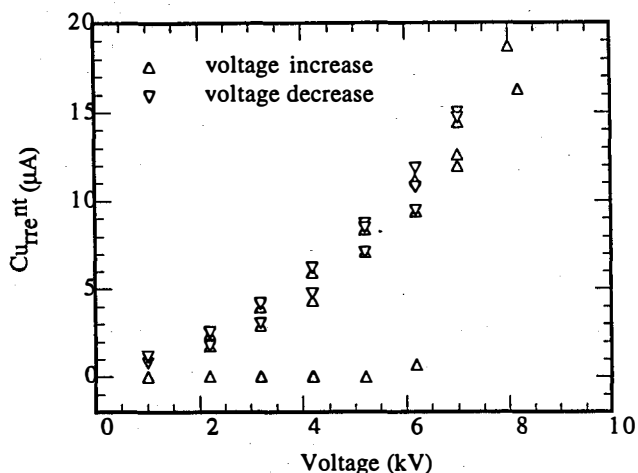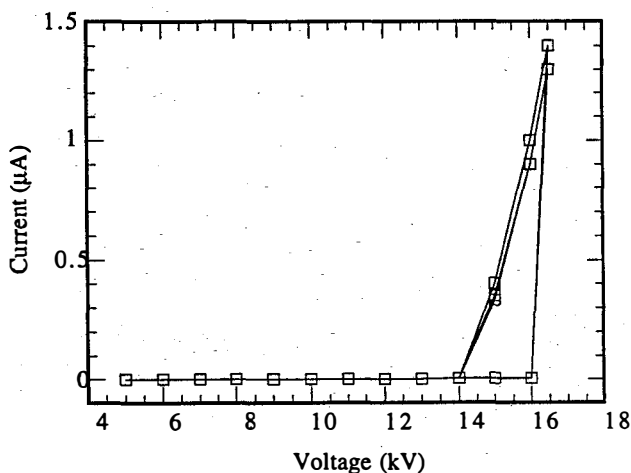
The surface energy obtained from the mechanical strength measurements for the sodium silicate bonding (2 wt.% at 90 °C) is around 2.6 J/m^2, which is comparable to the value of 2.2 J/m^2 obtained in conventional wet oxidized silicon direct bonding at 1400 °C [12], and also is comparable to the value of 3 J/m^2 obtained in the low temperature silicon wafer bonding with sodium silicate at > 200 °C [9]. The high temperature direct

bonding gives a surface energy of around 6.7 J/m^2 which is close to the virgin glass fracture energy [13].

CONCLUSION

The low temperature bonding process has provided strong bonds between glass surfaces and good channel sealing for liquid phase analysis. Further applications in fabricating various devices for chemical and biological analysis are under investigation.

ACKNOWLEDGEMENTS

REFERENCES

1. D.J. Harrison, A. Manz, Z. Fan, H. Lüdi, and H.M. Widmer, "Capillary Electrophoresis and Sample Injection Systems Integrated on a Planar Glass Chip", *Anal. Chem.*, *64*, 1926 (1992).
2. A. Manz, D.J. Harrison, E. Verpoorte, J.C. Fettinger, A. Paulus, H. Lüdi, and H.M. Widmer, "Planar Chips Technology for Miniaturization and Integration of Separation Techniques into Monitoring Systems. Capillary Electrophoresis on a Chip", *J. Chromatogr. 593*, 253 (1992).
3. S.C. Jacobson, R. Hergenröder, L.B. Koutny, R.J. Warmack, and J.M. Ramsey, "Effects of Injection Schemes and Column Geometry on the Performance of Microchip Electrophoresis Devices", *Anal. Chem.*, *66*, 1107 (1994).
4. S.C. Jacobson, R. Hergenröder, L.B. Koutny, and J.M. Ramsey, "Open Channel Electrochromatography on a Microchip", *Anal. Chem.*, *66*, 2369 (1994).
5. A.W. Moore, Jr., S.C. Jacobson, and J.M. Ramsey, "Microchip Separations of Neutral Species via Micellar Electrokinetic Capillary Chromatography", *Anal. Chem.*, *67*, 4184 (1995).
6. A.T. Woolley and R.A. Mathies, "Ultra-High-Speed DNA Fragments Separations Using Microfabricated Capillary Array Electrophoresis Chips", *Anal. Chem.*, *67*, 3676 (1995).
7. S.C. Jacobson and J.M. Ramsey, "Integrated Microdevices for DNA Restriction Fragment Analysis", *Anal. Chem.*, *68*, 720 (1996).
8. S.C. Jacobson, R. Hergenröder, A.W. Moore, Jr., and J.M. Ramsey, "Precolumn Reactions with Electrophoretic Analysis Integrated on a Microchip", *Anal. Chem.*, *66*, 4127 (1994).
9. H.J. Quenzer and W. Benecke, "Low-Temperature Silicon Wafer Bonding", *Sensors and Actuators A, 32* , 340 (1992).
10. J.H. Schneibel and M.G. Jenkins, "Slow Crack Growth at Room Temperature in FeAl", *Scripta Metallurgica et Materialia, 28*, 389 (1993).
11. L. Holland, "The Properties of Glass Surfaces", John Wiley & Sons Inc., New York, 1964, Chapter 9, p456.
12. W.P. Maszara, "Silicon-on-Insulator by Wafer Bonding: A Review", *J. Electrochem. Soc., 138*, 341 (1991).
13. R.W. Davidge and G. Tappin, "The Effective Surface Energy of Brittle Materials", *J. Mater. Sci., 3*, 165 (1968).

OPTIMIZATION OF LOW TEMPERATURE NH₃ PLASMA ACTIVATED DIRECT BONDING

R.W. Bower, W. Chan, L. Hong, L. LeBoeuf, A. Li , and J. Lee
University of California, Davis
Davis, CA 95616
bower@ece.ucdavis.edu

ABSTRACT

Previous work has described the existence of low temperature NH_3 plasma activated direct bonding but has not provided the details that allow this technique to be applied to a variety of microstructure applications. This paper describes the standard surface preparation and optimization of the NH_3 plasma activation for low temperature silicon bonding. Procedures discussed include cleaning, wafer handling, plasma activation, bonding, and annealing. Critical parameters investigated in the NH_3 plasma treatment are flow rate, power, and time. The optimal setting is 75 sccm, 50 W, and 5 minutes.

INTRODUCTION

Low temperature NH_3 plasma bonding has been described in earlier publications [1, 2, 3]. Applications of these techniques have been have also been described [4]. Mechanical considerations have also been described in detail [5]. While these publications have described the basic concepts and applications of this technology the details of practicing and optimizing this technique have not been presented. This paper gives a detailed description of the practice and optimization of this technique.

EXPERIMENTAL PROCEDURES

Criteria for successful direct silicon to silicon bonding include consideration of the flatness, waviness, and roughness of the material. For this optimization experiment, wafers with a radius of curvature greater than 100 m, roughness less than 1 nm, and a waviness parameter greater than 10^{-6} were used. By meeting these material characteristics, the stress induced by bonding will not exceed $\sigma_i = 10^{-6}$ which ensures a conformal pair [5].

The cleaning procedure consists of a standard RCA clean comprised of the following: base bath [NH_4OH-H_2O_2-H_2O (1:1:7)] and acid bath [HCL-H_2O_2-H_2O (1:1:6)] without a subsequent BOE dip. Samples were handled with only vacuum tweezers to prevent possible damage to the surface. The silicon samples were prepared for bonding by activating the surfaces in an NH_3 plasma using a Technics PECVD Series 900. The bonded pairs were annealed for 20 hours at 300° C.

The parameters investigated in this optimization process were the flow rate, power, and time for the NH_3 activation as seen below:

Flow Rate (sccm)	Power (W)	Time (min)
35	50	5
55	125	10
75	200	15

A 3 x 3 x 3 experimental matrix was created. Six sample sets were prepared for each matrix element. The bonds were rated after the anneal cycle using a classification system of 0 to 5, with 5 being a bond without any voids. See table 1 for description of classification system.

Rating	Description
0	No Bond
1	Multiple fringe patterns
2	soft bond, or small region (spot) of solid bond, bond strength ~ 200 ergs/cm²
3	Solid bond to 1/3 of contact area, soft elsewhere, bond strength ~ 500 ergs/cm²
4	Solid bond to 2/3 of contact area, fringe patterns at edges, bond strength ~ 750 ergs/cm²
5	99.9% bonded area, void free, bond strength ~ 1000 ergs/cm²

Table 1: Bond Classification

An example of a type 5 bonded pair is shown in the TEM in Figure 1. This figure illustrates the two silicon chips with an oxide formed on each surface during the cleaning procedure. The total thickness of the oxide is 90 angstroms. Localized micro-voids can be seen along the bonded interface. This TEM is comparable to the quality achieved under high temperature bonding.
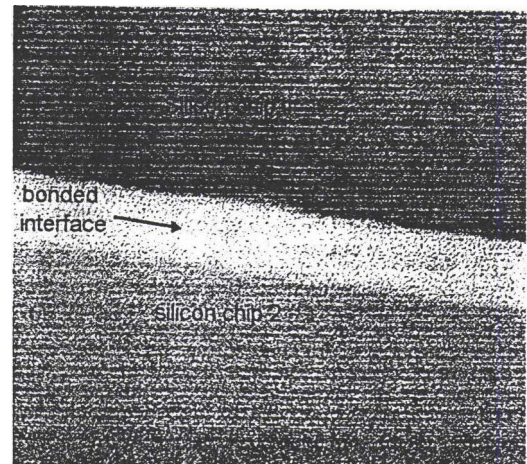

Figure 1: TEM of a type 5 silicon bonded pair. Magnification 370K

RESULTS & ANALYSIS

The optimal condition was found to be 75 sccm, 50 W, and 5 min. with an average rating of 4.2 and a bond strength of about 750 ergs/cm^2. In Table 2, the averages and binomial distribution are shown for the other elements of the matrix. This setting was analyzed statistically using a binomial distribution. Taking into consideration the bonding and quality probabilities, the statistical analysis proposes that there is a 33.5 % probability of finding consistent high quality bond characteristics in this group as compared to the other groups. These statistics are indigenous to each trial, meaning they are relative and not absolute. It shows how the results of each trial compare to the others and not to the overall experimental run.

35 sccm	50 W	125 W	200 W
5 min	-	-	2.33, .01%
10 min	-	-	2.00, .01%
15 min	-	-	1.67, 01%
55 sccm			
5 min	2.08, .05%	-	-
10 min	2.42, .01%	-	3.42, 2.9%
15 min	1.50, 0%	-	-
75 sccm			
5 min	4.12, 33.5%	-	3.83, 1.6%
10 min	4.00, 1.6%	-	-
15 min	2.83, .05%	-	-

Table 2: Average rating and binomial distributions for experimental conditions. These were computed only for averages greater than 1.

CONCLUSION

Optimization of low temperature NH$_3$ plasma activated direct silicon bonding was investigated and determined to be 75 sccm, 50 W, and 5 min. The optimized parameters found produced a substantially higher probability of finding consistent high quality bonds than the other conditions investigated.

REFERENCES

1. R. W. Bower, M. S. Ismail and B. E. Roberds, *Appl. Phys. Lett., 28 June 1993 pp. 2485-3487.*
2. R. W. Bower, M. S. Ismail, B. E. Roberds and S. N. Farrens,. Journal of Transducers 93 June (1993).
3. W. Bower and M. S. Ismail. NITROGEN BASED LOW TEMPERATURE DIRECT BONDING. Filed June 23, 1992, in issue June 1995.
4. R. W. Bower, V.H.C. Watt, R. Sundararaman and W. Chan, 1994 ISHM Symp., Boston., MA, Nov. 15-17.
5. R. W. Bower, W. Chan, L. Hong and V. H. C. Watt, Journal of the Electrochemical Society, Oct. 1995.

AN INTEGRATED ACCELEROMETER AS A DEMONSTRATION OF A NEW TECHNOLOGY USING SILICON FUSION BONDING AND DEEP REACTIVE ION ETCHING

J. Mohan,[2] N. I. Maluf,[1,2] K. E. Petersen,[2,3] and G. T. A. Kovacs[2]
[1]Lucas NovaSensor, 1055 Mission Court,
Fremont, CA 94539

[2] Stanford University, Center for Integrated Systems,
Stanford, CA 94305-4075

[3] Cepheid, 3655 Valley Ridge Lane,
San Jose, CA 95148

ABSTRACT

An all single crystal silicon accelerometer fabricated using silicon fusion bonding (SFB) and deep reactive ion etching (DRIE) is presented. The device integrates an interdigitated micromechanical sense element with simple CMOS circuitry. The capacitive sense plates are 60 µm deep with an aspect ratio of 15 to 1. Preliminary testing has shown that large changes in capacitance (> 100 fF) are achievable. A sensitivity of 90 mV/g was demonstrated using off-chip commercially available IC's.
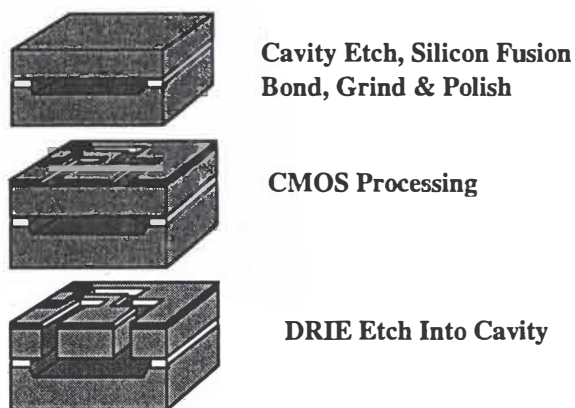
Cavity Etch, Silicon Fusion Bond, Grind & Polish

CMOS Processing

DRIE Etch Into Cavity

Figure 1: A simplified schematic illustrating the major process steps.

INTRODUCTION

A new process was recently presented[1] combining silicon fusion bonding (SFB) and deep reactive ion etching (DRIE) for the fabrication of high aspect ratio, single crystal silicon microstructures. It combines the many advantages of "surface" micromachining, namely design flexibility and compatibility with conventional IC fabrication processes, with those of traditional "bulk" micromachining, namely robustness and three-dimensional shaping. The process involves two major steps for the fabrication of the mechanical microstructures: a shallow etch and silicon fusion bonding are used at the beginning to form an embedded cavity, and a deep reactive ion etch down to the cavity is used at the end to release the microstructures. Signal processing circuitry is fabricated using conventional IC fabrication processes between the SFB and DRIE steps (Fig. 1). To demonstrate the capabilities of the SFB/DRIE technology, an accelerometer was fabricated integrating a mechanical sense element with simple signal processing circuitry.

DESCRIPTION

The interdigitated micromechanical sense element (Fig. 2) takes advantage of the fact that beams fabricated using the above process are compliant in the plane of the die but very stiff in perpendicular directions (Fig. 3) thus minimizing cross-axis sensitivity. Furthermore, the deep etching allows the fabrication of substantially larger proof masses and capacitances than possible using surface micromachining processes. The device typically uses four sets of interdigitated plates, two configured as a capacitive half-bridge for sensing the displacement, and two for electrostatic actuation (Fig. 4). Separating the sense plates from the actuation plates allows large sense signals to be used and thus improves the noise performance for
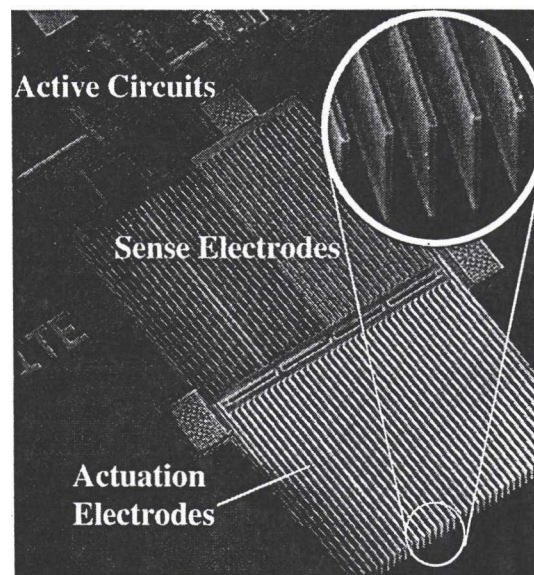
Figure 2: A scanning electron micrograph of a cleaved device showing the interdigitated sense element and part of the surrounding circuitry. The inset shows a magnified image of the high aspect ratio plates. The micromechanical element is 1.5x1.0 mm² with an overall capacitance of ~ 6 pF.

closed loop. The beams were all 6 µm wide with a spacing of 4 µm and a depth of 60 µm. The overall sense capacitance ranges between 2 to 6 pF depending on the size of the element with a change in capacitance per unit of acceleration ranging between 30 and 150 fF/g. Due to the large proof masses (30 to 60 µg), the resonant frequency was less than 3 kHz.

Figure 3: A scanning electron micrograph showing the set of plates attached to the shuttle plate and the edge of the supporting spring. The plates are compliant only in the plane of the die.

RESULTS

Sense and amplification circuitry was designed and integrated with the micromechanical structures using the Stanford p-well CMOS process. Various building blocks including amplifiers, buffers and a simple demodulator were tested and found to be functional. Due to the large available capacitance, preliminary testing was completed using external circuitry with the accelerometer in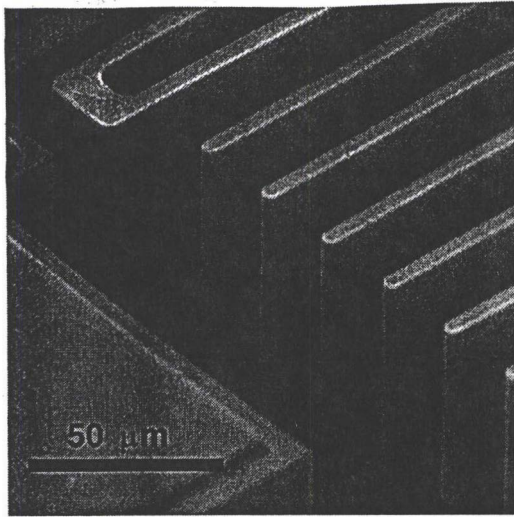 open loop. A 100 kHz, 40 mV p-p signal was applied to the capacitive half-bridge and the current imbalance was amplified by means of an I-V converter (Linear Technology LT1056) and rectified using a synchronous demodulator (Analog Devices AD630). The accelerometer was mounted alongside a reference accelerometer (for calibration purposes) on a shaker motor and the signals from both devices were recorded. The results, shown in Fig. 5, indicate a sensitivity of 90 mV/g. A minimum resolution of better than 50 mg was measured. This figure is determined by the electronic interface rather than the mechanical performance of the sense element. Mechanical noise figures are estimated at less than 0.2 mg/$\sqrt{Hz}$. Non-idealities, including non-linearity, are currently being characterized and their sources examined. Change in the capacitance of the sense plates as a function of an electrostatic bias applied to the actuation plates was also measured (Fig. 6). As expected, a non-linear behavior was obtained in reasonable agreement with the results of a simple model using parallel plates. Depending on the stiffness of the supporting spring and the number of biased plates, the "collapse" voltage varied between 3.5 and 25 V.
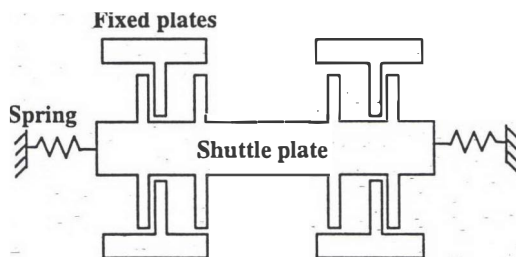
Figure 4: A schematic illustrating the basic mechanical sense element.
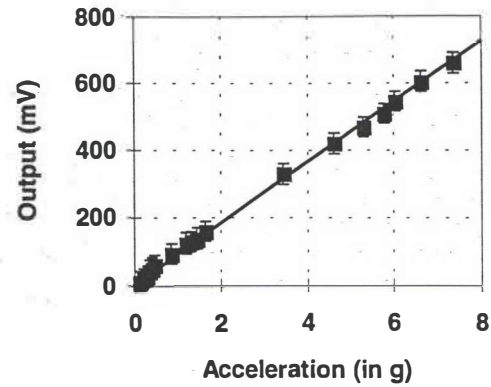
Figure 5: A graph showing the accelerometer measured output voltage as a function of externally applied acceleration.
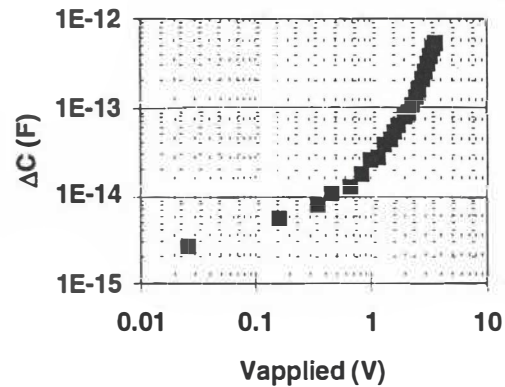
Figure 6: A graph showing change in capacitance as a function of an externally applied electrostatic bias. The base capacitance for this particular device is 3.6 pF. The collapse voltage is >8 V.

SUMMARY

An accelerometer fabricated using silicon fusion bonding and deep reactive ion etching was presented. The device demonstrates the process capabilities of merging SFB and DRIE for the fabrication of high aspect ratio mechanical microstructures. Ease of integration of signal processing circuitry using conventional CMOS was also demonstrated.

REFERENCES

1. E. Klaassen, K. Petersen, J. M. Noworolski, J. Logan, N. Maluf, J. Brown, C. Storment, W. McCulley, and G. Kovacs, "Silicon Fusion Bonding and Deep Reactive Ion Etching; A New Technology for Microstructures," in the proceedings of the 8th International Conference on Solid-State Sensors and Actuators, Transducers '95, Stockholm, Sweden, June 1995, p. 556

ACKNOWLEDGMENTS

ANISOTROPIC SINGLE CRYSTAL SILICON ETCHING
IN HIGH DENSITY RFIC PLASMA
WITH HIGH ASPECT RATIO AND HIGH SELECTIVITY

Tam Pandhumsoporn and Keven Yu
Alcatel Comptech, Inc.
550 Parrot Street, San Jose, California 95112

ABSTRACT

A high density Radio Frequency Inductively Coupled (RFIC) plasma etcher has been used to etch single crystal silicon with high aspect ratio and high selectivity. Silicon etching with fluorine based simple chemistry and controlled temperature of the wafer has been investigated on etch rate, trench profiles and selectivity. The trade-off of each process parameter to end result is a well-known phenomenon in the etch technology. Silicon etch rates up to 8 microns/min have been achieved with good results and extremely high selectivities to thermal oxide that range from 200 -1000. High aspect ratios, greater than 30:1, have also been achieved with very vertical profiles. This type of process performance has been offered for both new and existing applications, such as (microelectro-mechanical systems) MEMS devices, high-voltage isolation devices and semiconductor IC's. This paper reviews some of the plasma etching fundamentals and some of the complexities associated with RFIC etching.

INTRODUCTION

Silicon trench etching plays an important role in a wide range of applications in IC and MEMS device fabrication. A quick review of traditional semiconductor IC silicon etching requirements compared to MEMS etching requirements reveals the need to expanding into a truly three dimensional etching technology for MEMS devices. These three dimensional requirements in a MEMS device increase the importance of understanding and optimizing the trade-offs typically seen between each etch process parameter.

Current IC Approach	MEMs Approach
Surface etching	Bulk etching
Feature size < 1μ	Feature size 1μ - > 100μ
Etch deep < 10μ	Etch deep 10μ- 600μ or through wafer
Etch on single wafer	
Etch on one side	Etch on single and bonded wafers
	Etch on single and both wafer sides.
Etch rate < 1μ/min	Etch rate > 2μ/min
Oxide selectivity > 20:1	Oxide selectivity 100:1
Aspect ratio < 10:1	Aspect ratio > 10:1
Toxic and corrosive gases (Chlorine and Bromine chemistries)	Non toxic and non corrosive gases (Fluorine Chemistries)
Require special facility installation, such as scrubber, gas cabinet and pumping system	Less requirement on facility installation

EXPERIMENTAL

The wafers used for this work are silicon substrate, P type, {100} orientation, pre-patterned with a variety of materials by a wafer supplier. The wafers' sizes range from 100 mm to 150 mm. An Alcatel 602E system is used for this investigation. A member of the Alcatel 600 modular family of vacuum systems, the major components of the Alcatel 602E include a process chamber, load lock, transfer chamber, pumping system and electrical and computer control units. The system features a vacuum cassette load lock with robotic transfer of wafers between the cassette and the single wafer process chamber. Plasma etching of the wafers is performed on a temperature controlled pedestal, which can be varied from -120 C to +20 C. The plasma source uses a patented RFIC source design that generates a high density plasma (up to 10^{12} ions/cm^3 in argon) at a low pressure of about 10 mTorr. Substrate bias is separately applied with another RF power supply at 13.56 MHz. Fluorine based chemistries are controlled by mass-flow controllers. A variable conductance gate valve controls the process pressure. A set of permanent magnets in the process chamber walls magnetically confine the plasma. Process parameters were varied as follows: pressure range from 10 to 30 mTorr, plasma source power from 500 to 1400 watts, gas flow rate up to 200 sccm, pedestal temperature range from -120 to +20 C and substrate bias from -20 to -80 volts. Mask materials used were thermal oxide, CVD oxide, low temperature oxide, silicon nitride and photoresist. The mask openings were etched by dry etching and the feature sizes ranged from sub-micron to a few hundred microns. The etch depths and profiles were determined by an Hitachi SEM and a Dektak profilometer.

RESULTS AND DISCUSSION

To etch silicon, SF$_6$ was used because of its ability to ionize easily under an RF discharge, giving a lot of radicals F*, which are the main silicon etching species [1]. The anisotropic etching mechanism has been extensively studied and discussed. The etching chemistries based on fluorine and O$_2$ addition produce a passivation layer on the sidewalls of the feature during the etching [2]. This thin oxide passivation layer protects the sidewalls from attack of the fluorine neutrals. As such, a truly vertical anisotropic silicon etch can be successfully achieved. In the case of fluorocarbon chemistries used, a polymerized fluorocarbon layer deposits efficiently under low temperature and the polymer passivates the sidewall, controlling lateral silicon etching[3]. Both techniques have been proven to be very effective for control of sidewall erosion during etching. It is important to understand the benefits and drawbacks of each of these two techniques in order to be able to optimize the etching parameters, thereby achieving the optimum process performance for any given application.

Surface charging can indeed develop due to an imbalance of electrons and ions. Negative profiles have been observed when silicon etching in high density plasma [4]. Obviously, increasing the sidewall passivation while increasing the ion energy should reduce the deflection and yield a more vertical profile.

An effect of substrate bias on mask selectivity has also been investigated. Thermal oxide is one of the best mask materials to be used for very deep silicon trench etching. It provides an extremely high selectivity that ranges from 200 to 1000. It is a good candidate for these MEMS applications because of its properties and the well-known technology for oxidation, patterning and mask opening. Higher substrate bias will reduce the mask selectivity, as shown in Fig. 1.
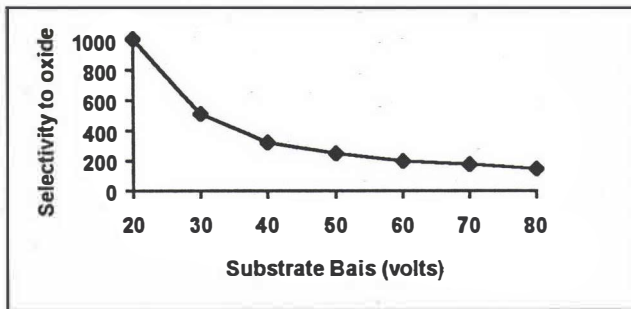

Fig. 1. An effect of substrate bias on selectivity to oxide

Different mask materials have been also investigated. The selectivity of silicon to these materials has been established as seen in the table below.

Mask Materials	Mask Selectivity to Silicon
Thermal oxide	200 - 1000
CVD oxide	20 - 50
Low temperature oxide	30 - 100
Silicon plasma nitride	20 - 50
Photoresist	30 - 100

The types of mask patterns and exposed areas play an important role in what type of process conditions are required for specific mask patterns. These etch characteristics are optimized through the combination of hardware configuration and process parameter adjustments. These allow the desired good results of anisotropic profiles, high etch rates and high selectivity to the mask to be achieved.

Various trenches and pillar structures have been studied to produce high aspect ratio, vertical profiles. Fig. 2(a) shows a SEM micrograph of sub-micron pillar features (0.6μm) with an aspect ratio greater than 30:1. Fig. 2(b) shows 1.5 μm pillars at 54 μm depth with truly vertical profile and smooth sidewalls. Finally, plasma source power is one of the dominant process parameters in terms of etch rate, as can be seen in Fig . 3.

CONCLUSION

High etch rates with high quality, high aspect ratio features have been achieved by using Alcatel 602E system. With this technology, very deep structures with high aspect ratios and very small feature sizes can be applied to new applications for both the MEMS and the semiconductor industries. A high mask selectivity allows the etching of a very deep silicon trench with a minimum mask thickness. The control of process parameters with optimal hardware is essential to produce the best quality etch result.
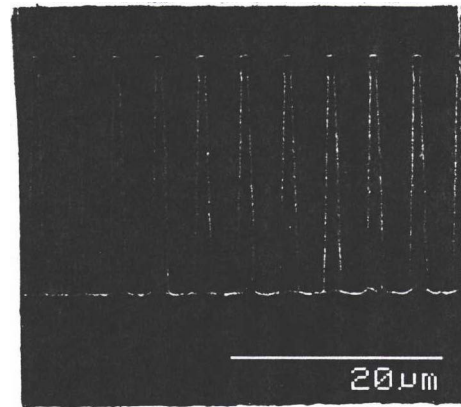
Fig. 2. (a) a SEM micrograph of 22 μm depth submicron pillars with >30:1 aspect ratio.
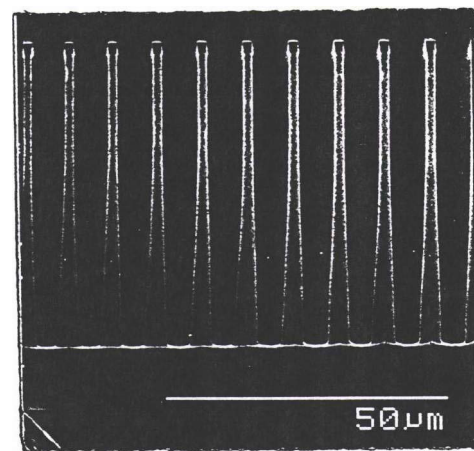
Fig. 2. (b) a SEM micrograph of 54 μm depth of 1.5 μm pillars.

Fig. 3. Effect of source power on etch rate

REFERENCES

[1] E. Cabruja, Sensors and Actuators A, 37-38 (1993) 766.
[2] H.H. Wang, Plasma etching of poly Si in SF_6 -O_2 mixtures, Prc. Int. IEEE V-MIC Conf., June 25-26 1985, pp 335-341.
[3] Shinichi Tachi, J. Vac. Sci. Technol. A9 (3), 1991.
[4] S. Murakawa, Appl. Phys. Lett. 64, 1558 (1994).

Side-wall Feature Definition For Through-wafer Interconnects Using 45° Mirror Surfaces

Chang Liu†, Mark A. Shannon† and Ilesanmi Adesida

Microelectronics Laboratory, 208 N. Wright Street
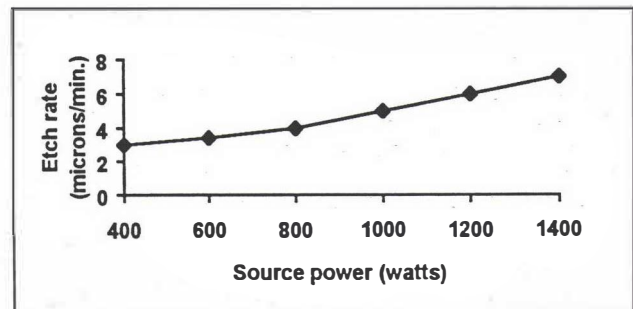†Mechanical and Industrial Engineering Department, 1206 W. Green Street
University of Illinois at Urbana-Champaign, Urbana, IL 61801

ABSTRACT

A novel scheme of patterning vertical chip surfaces using a 45° mirror structure has been explored. We demonstrate, for the first time, straight line paths on the vertical edges of diced wafer chips to achieve front-to-back electrical interconnection; these present significant advantages in packaging MEMS systems. Photoresist is electroplated uniformly on all surfaces (including sidewalls); it is then exposed with collimated UV-light beam reflected off a 45° mirror surface placed near the side walls. The minimum line-width resolution is limited by shadow-mask diffraction and mirror-surface scattering; currently the line width loss is on the order of 25 μm with a 320-nm UV light source.

INTRODUCTION

Traditionally, microelectronics chips are packaged in an enclosed environment and bonding wires are used to connect bonding pads to pins on a package. Many MEMS sensors and actuators are, however, directly exposed to the physical environment and the traditional IC packaging scheme will present problems. In many MEMS applications (e.g. fluid mechanics and bio-medicine), exposed bonding wires can have serious disadvantages: bonding wires can disturb the physical environment and are subjected to physical damages. For instance, a shear-stress sensor based on thermal-transfer principles [1] must be placed flush with the wind-tunnel surface; any surface protrusions (such as bonding wirings) will be highly undesirable.

As one alternative, wafer through-hole interconnects have been demonstrated [2–4]. These are fabricated using an-isotropic silicon etching to obtain through-wafer holes bound by {111} surfaces. There are two major disadvantages. First, the hole opening on the backside of the silicon wafer is typically several hundred micrometers wide; it consumes large space, renders the wafer fragile and generally prohibits further processing. Secondly, the through-wafer hole typically takes approximately 10 hours to complete using wet etchant; the time consumption will not allow the wide use of such a technique for today's large-sized ($\geq$ 6in diameter, and therefore thick ($\geq$ 500 μm in thickness) silicon wafers.

We propose a novel scheme for achieve front-back interconnection - by patterning metal leads on the vertical edges of the diced silicon chips. With this new technology, interconnects take little space and can be made in a much shorter time. Density of interconnects can be potentially higher than previously mentioned methods.

In high-density packaging where chips will be in contact with each other, interconnect paths can be recessed to prevent electrical shorting; recess structures can also be achieved with this patterning technology. This new exposing scheme can potentially be applied to pattern sidewalls *within* a wafer and create three-dimensional MEMS structures to achieve added processing flexibility and device functionality.

SCHEMATIC

The schematic of the exposure setup is shown in Fig. 1. A *mirror chip* with a 45° mirror surface is placed next to a *device chip* to be patterned. Incoming collimated UV light beam (inside a contact aligner system) is reflected off the 45 ° mirror surface and directed toward the photoresist material on the sidewall of the device chip. Due to the light beam diffraction and mirror-surface scattering, it is advantageous to place the two chips as close as possible in order to achieve optimum resolution. In industrial applications, a pre-manufactured frame with four mirror surfaces facing inward can be placed outside of a device chip and expose all four edge surfaces and the front surface simultaneously.
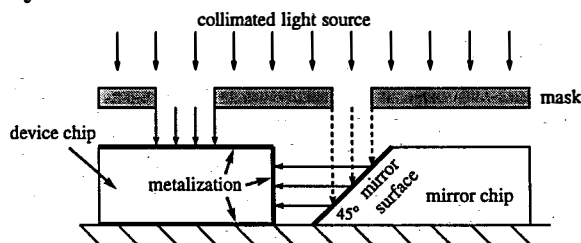

Fig. 1 Schematic diagram of exposing side-wall photoresist with a 45-degree mirror surface.

SAMPLE FABRICATION

A silicon device chip (500 μm in thickness) with smooth edge surfaces is used. These vertical surfaces can be created using proper wafer dicing techniques. The metal layer is either evaporated aluminum or electro-less deposited Ni or Cr (Transene Co.) In the first case, Al is evaporated separately on the front/back surfaces and side-walls. The chip is then placed in a photoresist electroplating bath (positive working PEPR 2400 from Shipley Co.) to grow approximately 2 μm of resist; it is then baked at 120 °C using a convection

oven. A special chip holder is used to avoid damages to the photoresist surfaces. The device chip and the mirror chip are placed immediately adjacent to each other on a vacuum chuck in a Karl-Suss contact aligner; the exposure is done under hard-contact mode.

MIRROR FABRICATION

A first 45° mirror is made from a blue tempered spring steel (SAE-1095) and the mirror surface is produced by conventional machining and finally mirror-polished using buffing wheels. Figure. 2 is an SEM micrograph of the finished mirror surface. The arithmetic mean roughness (Ra) over a 80 μm scan distance is measured to be 20-40 nm. Close SEM examination reviews micro-scale voids on the surface. We concluded this mirror surface is not adequate; in the future, polished optic glass can be used to improve this technique.
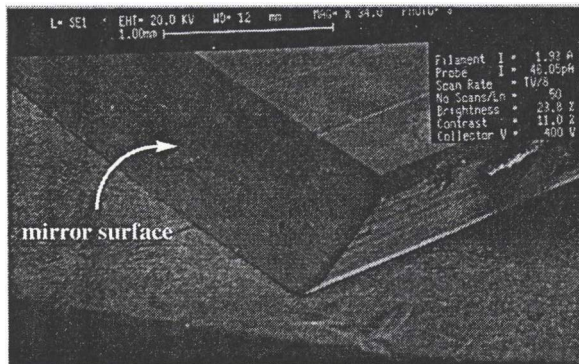

Fig. 2 SEM micrograph of the conventionally machined mirror surface.

Micro mirrors with atomic smoothness can be formed using an-isotropic etching [5, 6] of semiconductor substrates. Using silicon substrate, for example, the best optical quality is obtained by etching a silicon wafer unconventionally cut with a 9.7° offset to the <100> crystal orientation [6]. Unfortunately, wafers of this particular specification are not readily available. To demonstrate the principle of side-wall patterning, we used EDP etched {111} surfaces from <100> oriented, 500μm-thick wafers. The mirror surface is therefore 54.7° from the base plane and offset the deflected beam from the horizontal position; it is subsequently used to expose wafers that are no more than 400μm thick. The mirror surface roughness is 1–2 nm, significantly better than that of the conventional machined surface. To increase the surface reflectivity, high reflective metal (Al or Ag) can be evaporated in the future.

PATTERNING EXPERIMENTS

The minimum line width is determined by two factors: diffraction associated with shadow-mask proximity printing and light scattering at the mirror surface.

The minimum line width determined by diffraction (l_d) is

$$l_d \cong \sqrt{\lambda t}$$

where λ is the wavelength of the exposure radiation and t is the distance of the gap. Besides, l_d will not change with the vertical height because the optical path length is constant. In our experiments, $\lambda = 320$nm and $t \approx 500\mu$m, therefore the diffraction-limited minimum

line width is 12.6 μm. Mirror surface scattering contributes to expose intended masked region and causes a line-width loss. The exact amount will be linearly dependant on the horizontal distance from the mirror surface to the device chip edge. Detailed analysis will be presented elsewhere; detailed process can also be experimentally characterized [7].

Straight vertical interconnect paths, 50 μm in width, are shown in Fig. 3. The original line width on the mask is 100 μm; light beam expansion therefore accounts for 25 μm of line-width loss on each side. This is confirmed because original 50-μm wide lines disappeared near top surface of the device chip. Currently, we are improving on the optical exposure technology in order to obtain higher resolution, developing theories and design/fabrication guidelines.
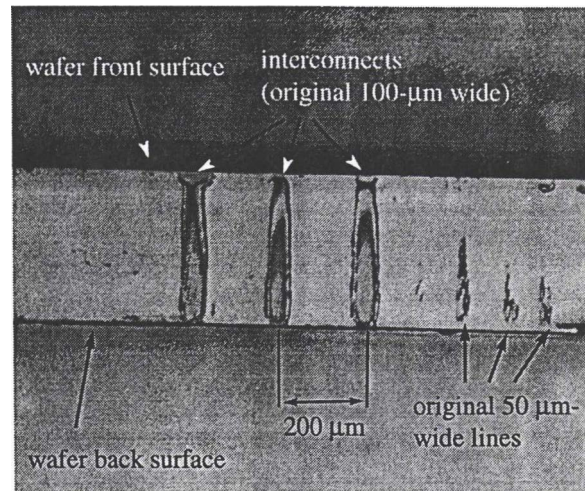

Fig. 3 Optical micrograph of interconnect paths on the sidewall of a 400 μm-thick silicon chip.

REFERENCE

1. C. Liu, et. al., "Surface micromachined thermal shear-stress sensors," *Proceedings, Symp. Application of Microfabrication to Fluid Mechanics, 1994 International Mechanical Engr. Cong. and Expo.*, Chicago, IL, p. 9, 1994.

2. S. Linder, et. al., "Fabrication technology for wafer through-hole interconnections and three dimensional stacks of chips and wafers," *IEEE Proc. MEMS'94*, p. 349, 1994.

3. H.D. Goldberg, et. al., "A silicon wafer-bonding technology for microfabricated shear-stress sensors with backside contacts," *Proc. Solid-State Sensors and Actuators Workshop*, Hilton Head, p. 111, 1994.

4. S. Linder, H. Baltes, et. al., "Photolithography in anisotropically etched groves," *Proc. IEEE MEMS'96*, p. 38, 1996.

5. C.H. Chen and S.C. Lee, "Monolithic integration of an AlGaAs/GaAs surface emitting laser diode and a photodetector," *Appl. Phy. Lett.*, 59(27), p. 3592, 1991.

6. C. Strandman, et. al., "Fabrication of 45-degree optical mirrors on (100) silicon using wet anisotropic etching," *Proc. IEEE MEMS'95*, p. 244.

7. V. Greco, et. al., "Characterization of the scattering properties of a mirror by speckle-field statistics," *Applied Optics*, 33(25), p. 6105, 1994.

DIRECT MEASUREMENTS OF YOUNG'S MODULUS AND TENSILE STRENGTH OF POLYSILICON

William N. Sharpe, Jr., Bin Yuan, and Ranji Vaidyanathan
Department of Mechanical Engineering,
Johns Hopkins University
Baltimore, Maryland 21218-2686

Richard. L. Edwards
Applied Physics Laboratory
Johns Hopkins University
Laurel, MD 20723-6099

ABSTRACT

Techniques and procedures have been developed for testing thin films under uniaxial tensile loading. Polysilicon specimens 3.5 μm thick are deposited on silicon wafers in the shape of a tensile specimen with a supporting frame. The specimen is released by etching away the silicon wafer under the tensile section only. The frame containing the specimen is mounted in a loading mechanism consisting of a linear air bearing, a load cell, and a piezoelectric translator. The supporting frame is then cut and the specimen loaded in uniaxial tension. Strain is measured by laser-based interferometry from two thin gold lines deposited on the specimen.

This approach enables measurement of Young's modulus in a <u>direct</u> manner consistent with its definition. Results are presented from two different manufacturing (MUMPS) runs at the Microelectronic Center of North Carolina (MCNC). the overall average of Young's modulus is 168 GPa ± 7.6 GPa, and the tensile strength is 1.25 GPa ± 0.16 GPa.

INTRODUCTION

Most measurements of the elastic and strength properties of polysilicon and other thin films have been by <u>indirect</u> methods, i.e. the measured quantity (usually deflection) is related to the applied load or pressure by an equation that includes the material property of interest. The standardized definition of Young's Modulus is given in the American Society for Testing and Materials (ASTM) standard E-111 which states, "The test specimen is loaded uniaxially and load and strain are measured, either incrementally or continuously."[1]. Further, ASTM E-111 requires that strain be measured <u>directly</u> on the specimen with suitable extensometers.

There have been measurements of mechanical properties of polysilicon that loaded the specimens uniaxially, but all recorded the relative displacement between the ends of the specimens and used it to compute the strain [2,3,4]. The measurements reported here are the first that fulfill the requirements of ASTM.

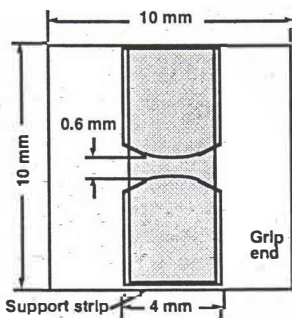## SPECIMEN PREPARATION AND HANDLING

Figure 1. Specimen schematic.

The material tested is phosphorus doped, LPCVD polysilicon deposited at MCNC. As such, it is representative of the material commonly used to form structural elements for surface micromachined MEMS devices. The specimen is deposited on a silicon wafer in the shape shown in Figure 1 with the tensile portion in the middle and two support strips on each side. The silicon die is 1 cm square and the specimen is 3.5 μm thick and 0.6 mm wide at its narrowest point. The wafer material beneath the tensile section and in the shaded area shown in Figure 1 is removed from the back of the die by anisotropic etching leaving the tensile polysilicon portion suspended between two grip ends that are connected by the support strips.

Figure 2 is a SEM photograph showing the specimen from an oblique view; there one can see the silicon wafer in the foreground and the polysilicon layer on top. The tensile specimen is stretched across the center of the photograph between the two grips.
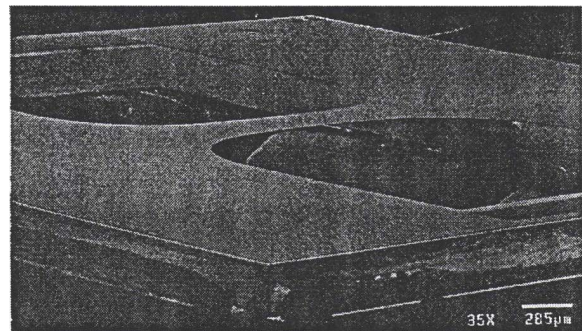

Figure 2. SEM photo after the substrate is etched away. The tensile specimen is in the middle of the picture.

STRAIN MEASUREMENT

Strain is measured with the Interferometric Strain Displacement Gage (ISDG) which is an optical technique for measuring the relative displacement between two reflective gage markers. For the polysilicon specimens, these two markers are gold lines that are deposited on the specimen during manufacture. Figure 3 is a schematic that illustrates the principle of the ISDG. The two gold lines are 0.5 μm high, 20 μm wide, 200 μm long and 300 μm apart.
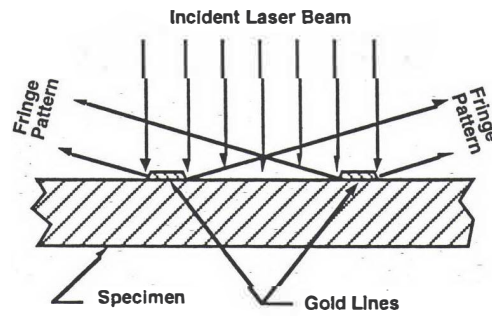

Figure 3. Schematic of the ISDG

When the gold lines are illuminated with a laser, the diffracted reflections from each edge of a line overlap and interfere to produce fringes. As the gage markers move relative to each other, the fringe patterns also move; their motion can be measured with photosensors and related to the relative displacement change generated by strain (or displacement if the lines are across a crack). Rigid-body motion will also cause the fringes to move, so it is necessary to average the movement of the two fringe patterns.

The principal attributes of the ISDG as used in these measurements is its non-contacting, non-reinforcing nature. The resolution is approximately 10 microstrain and the relative uncertainty is ± 3%. The ISDG is an established technique; a presentation of the optical principles as well as details of typical measurement systems is given in a NASA report [5].

TEST SYSTEM

The specimen, mounted in its carrier frame, is placed across a set of grips and the grip ends glued in place. One grip is fixed and the other one is attached to a linear air bearing whose slide connects to a load cell mounted on a piezoelectric actuator. This eliminates the friction in the loading mechanism and permits accurate measurements of the forces on the specimen. The piezoelectric translator has a range of 180 μm with a resolution of 0.09 μm and is controlled by the system microcomputer, i.e. the tests are conducted under displacement control. The load cell has a range of 1 lb with a resolution of 0.001 lb. The two support strips are then cut and the specimen is pulled to failure while recording the load and strain.

A schematic of the entire test system, absent the microcomputer that controls the loading and records the strain, is shown in Figure 4.
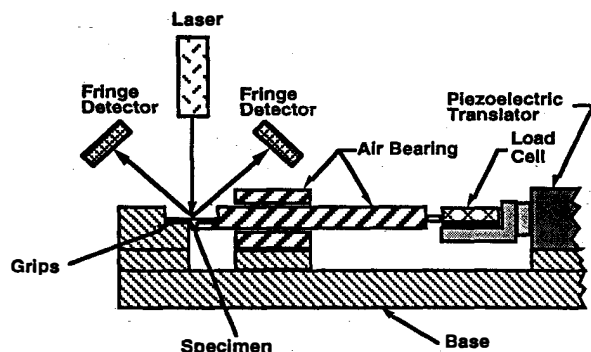

Figure 4. Schematic of the test system.

RESULTS

Figure 5 is a representative polysilicon stress-strain curve. The relative uncertainty in the stress arises primarily from the cross-section measurement and is ± 1% .

We have conducted 10 tests of specimens from the MUMPS 6 run and 9 on specimens from MUMPS 8.

	Young's Modulus GPa	Standard Deviation GPa	Tensile Strength GPa	Standard Deviation GPa
MUMPS 6	163	4.8	1.23	0.20
MUMPS 8	173	6.9	1.27	0.11
All Data	168	7.6	1.25	0.16

The Young's modulus compares well with other modulus measurements [3,6], while the mean tensile strength is lower than in polysilicon fibers [3], which may be due to either a size effect or the differences in the manufacturing process.
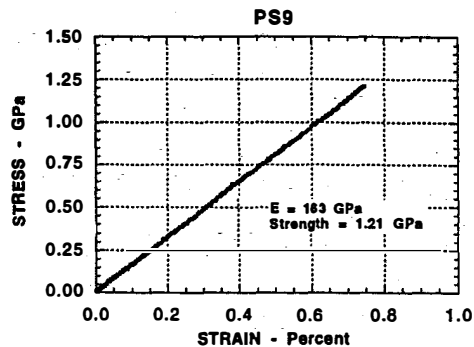

Figure 5. Representative stress-strain curve for polysilicon.

A statistical 't' test applied to the two groups of data shows that there is a statistically significant difference in the modulus values between the two manufacturing runs, but not in the strength values.

CONCLUSIONS

The reproducibility of the modulus speaks well for the test technique. The strength has a wider scatter, but this is to be expected in a brittle material. The measurements show that the manufacturing process is controlled.

This test system is able to solve the three main problems in conducting microsample tensile tests of extremely thin and fragile MEMS materials - ease of specimen preparation and handling, friction in the loading mechanism and accurate strain measurement.

The test techniques and procedures are now fully developed and can be used for important studies of new and existing materials that are used in MEMS.

ACKNOWLEDGMENTS

REFERENCES

1. "Standard Test Method for Young's Modulus, Tangent Modulus, and Chord Modulus", E-111, 1990 Annual Book of ASTM Standards, American Society for Testing and Materials, Philadelphia (1990), pp. 276-281.
2. J. A. Schweitz, "Mechanical Characterization of Thin Films by Micromechanical Techniques," *MRS Bulletin*, **17**, pp. 34-45 (1992).
3. J. Koskinen, J. E. Steinwall, R., Soave, and H. H. Johnson, "Microtensile Testing of Free-Standing Polysilicon Fibers of Various Grain Sizes", *Journal of Micromechanics and Microengineering*, **35**, pp. 13-17 (1993).
4. D.T. Read and J.W. Dally, "A New Method for Measuring the Strength and Ductility of Thin Films," *Journal of Materials Research*, **8**, No. 7, pp. 1542-1549 (1993).
5. W. N. Sharpe, Jr., "An Interferometric Strain/Displacement Measurement System", NASA Technical Memorandum 101638, (1989).
6. M. Biebl, T. Scheiter, C. Hierold, H. V. Philipsborn, H. Klose, "Micromechanics Compatible with an 0.8 mm CMOS Process," *Sensors and Actuators A*, **46-47**, pp. 593-597 (1995).

DESIGN AND IMPLIMENTATION OF LIGA FABRICATED, SELF-PRIMING IN-LINE GEAR PUMPS

Andrew S. Dewa, Keren Deng and Darren C. Ritter
Concis, L.L.C.
Vancouver, WA 98661

ABSTRACT

This paper presents the first self-priming, positive displacement micromachined pump. The in-line gear pump is a magnetically-actuated, two-gear plastic pump which is fabricated by the SLIGA process. The components of the pump are assembled and inserted in a tube, with the magnetic driving mechanism outside the tube. This method of magnetic actuation eliminates the seal issues. The preliminary test results show that the pump flow rate can be at least 70 μl/min. The pump pulls a vacuum at the inlet of at least 45 mm of water and is self-priming.

INTRODUCTION

There are many applications waiting for a viable MEMS based pumping system — a pump which is easily integrated into existing systems, requires no special skills to operate, and is easy to use. Some of these applications include micro analytical instrumentation, genetic engineering, protein synthesis, portable chemical and biological sampling systems, drug delivery, and environmental monitoring. To take these application out into the field, it is critical that the MEMS pumping system improves the usability of the instrument, along with reduce weight and volume, decrease power consumption, and reduce costs.

There have been a number of MEMS based liquid pumps published in the literature. Most are silicon based diaphragm pumps utilizing a many different inlet/outlet valves and actuation methods. The published literature on MEMS pumps can be summarized as a group: no self-priming liquid pumps have been reported. This is truly the limitation on commercialization of MEMS pumps, since requiring the technician in the field to prime the MEMS based pump in the instrument will override any advantages of MEMS fabrication.

The in-line pump is a LIGA fabricated, magnetically-actuated, gear pump which is designed to be inserted in a tube, and driven by an external magnetic field. The design philosophy of the in-line gear pump provides unique advantages for a micromachined pump. First, the seal problem is eliminated, since the whole pump body is in the fluid path. This includes both static seals for the pump body and moving seals for a driving mechanism. In fact, since the magnetic actuation is coupled through the tube walls, the fluid in the tube remains completely isolated from the environment. Therefore, actuation mechanism will minimize heating the fluid. Since the driving mechanism is not part of the pump itself, the pump can be made much less complex. This allows the pump to be disposable. Furthermore, for biomedical application, the pump and the tube can be sterilized together, without the drive mechanism. An added advantage is that the drive is reusable, reducing the cost of the ownership. Some of the target applications include: IV drug delivery, biomedical instrumentation, clinical analyzers, chemical instrumentation, and any applications where it is critical that the fluid path isolated from the environment.

This actuation scheme also provides a method for magnetic coupling of eccentric rotors with a nearly constant torque transmitted to the rotor. The driving method provides coupling with air gaps much larger than that reported for micromechanical rotational devices (i.e., magnetic micromotors). The coupling method demonstrated with the in-line pump allows the development of many new rotationally coupled micromechanical mechanisms and systems.

IMPLEMENTATION OF THE IN-LINE GEAR PUMP

Figure 1 is an exploded view of the gear pump. The inlet and outlet plates, the cavity plate, and the driving and driven gears are all fabricated via the SLIGA process using PMMA as the structural material[1,2]. Since the PMMA is the structural part, thickness control, surface finish and parallelism are critical for this device. In this case of the in-line pump, the gears are fabricated to 2-4 μm thinner than the cavity plate. The 78/22 Ni/Fe permalloy bar is also fabricated by the SLIGA process and is a further 2-4 μm thinner than the gears.
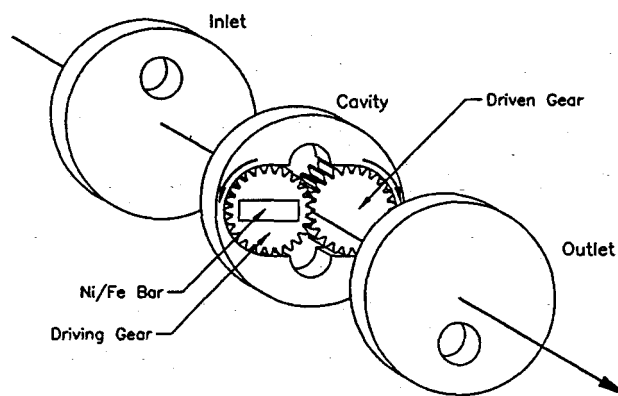

Figure 1: An exploded view of the gear pump. The inlet, outlet, cavity and gears are plastic fabricated using the SLIGA process. The pump gears are 24 tooth gears with a pitch diameter of 1.392 mm. The inlet and outlet ports are 0.696 mm in diameter. The driving gear contains a electroplated 0.3mmx1.0mm Ni/Fe bar for magnetic coupling.

Figure 2 shows the plan view and a cross sectional view of the pump/magnetic coupling structure. The micromechanical pump body is located in a tube, 1/8" ID 3/16" OD plastic, surgical grade tubing. The pump body is 1/8" OD to match the tubing. The tube is clamped in place by a bearing which is connected to the rotational magnetic coupling. The coupling consists of two permanent magnets bonded to a ring made of a material with a high permeability, to complete the magnetic path. The air gap is large relative to the scale of the micromechanical device.

One feature of this gear pump design, by stacking stages (i.e., alternating pump cavities and end plates), the outlet pressure head of the pump can be increased roughly proportionally to the number of stages, until the limits of the width of the magnetic coupling or the ultimate pressure limit of the pump seals is

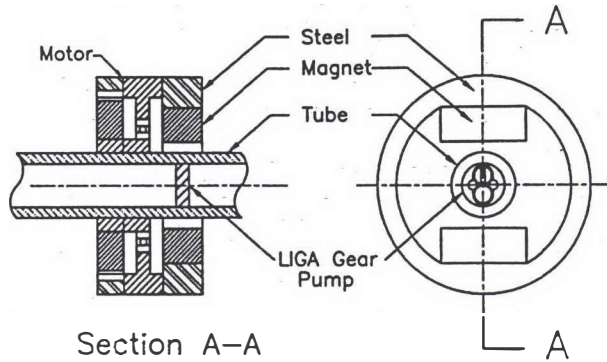reached. For correct operation, the driving gear in successive stages must alternate sides.

Figure 2: Plan view and cross sectional view of the LIGA gear pump with magnetic coupling structure of in-line gear pump. The tubing containing the micromechanical gear pump is clamped in a bearing which supports the rotating magnetic coupling.

Figure 3 shows an assembled in-line gear pump. The total thickness of the pump is 600 μm, 200 μm each for the two end plates and the cavity. The outside diameter of the pump body (inlet, outlet and cavity plates) is 1/8th on an inch (3.1750 mm). The inlet and outlet ports are 0.696 mm in diameter. The pump gears are 24 tooth gears with a pitch diameter of 1.392 mm. The driving gear has a 78/22 Ni/Fe permalloy bar centered in it of size 0.3 mm by 1.0 mm. The magnetic drive mechanism is fabricated carbon steel to which the permanent magnets are bonded.

2-D FEM simulations of the magnetic coupling in the in-line gear pump structure are used to verify the design concept. The maximum coupling torque of 12.4 μN-m is generated when the Ni/Fe bar is 45° to the magnetic field. The variation of torque throughout the rotation of the coupling at a fixed angle between the Ni/Fe bar and the magnetic field is less than 7%. Thus, uniform, magnetically coupled torque is produced.

The preliminary experimental results show that the gears could be driven at rotation speed of 3500 rpm, limited by test set up. The in-line pump produces flow rates of at least 70 μl/min. Most significantly, the in-line pump proves to be self-priming. The gear pump created a suction at the inlet tube of at least 45 mm of water. Further testing is underway to determine pressure head and flow rate limits, and as well as refined estimate of the suction.

CONCLUSIONS

This paper presents the first self-priming micromechanical liquid pump. The SLIGA-fabricated, magnetically-driven gear pump produced a suction of 45 mm of water at its inlet. The preliminary hydraulic data indicate that the pump is capable of generating flow rates of at least 70 μl/min. The in-line pump is inserted into tubing and the magnetic actuation is coupled through the tube walls, which eliminates the pump and connector seal issues and isolates the fluid from the environment.
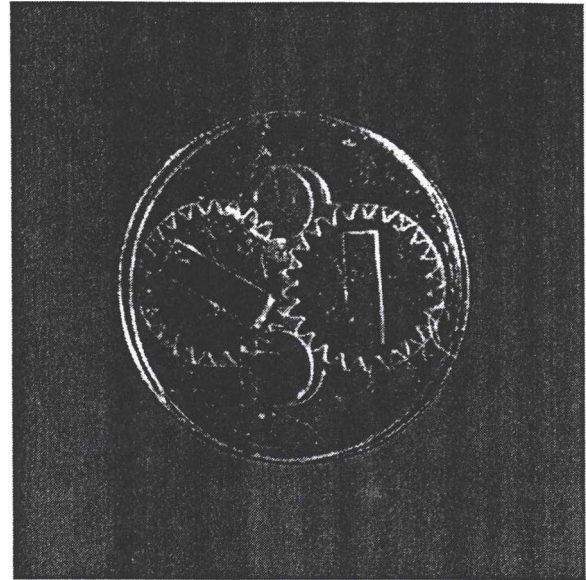

Figure 3: An optical photograph of an assembled in-line gear pump fabricated by SLIGA. The total thickness of the gear pump is 600 μm, 200 μm each for the two end plates and the cavity.

ACKNOWLEDGMENT

REFERENCES

[1] H. Guckel, T.R. Christenson, and K. Skrobis, "Metal Micromechanisms via Deep X-Ray Lithography, Electroplating, and Assembly," *Proceedings of Actuator '92*, Bremen, Germany, June 1992, pp. 9-12.

[2] H. Guckel, T.R. Christenson, T. Earles, J. Klein, J.D. Zook, T. Ohnstein, and M. Karnowski, "Laterally Driven Electromagnetic Actuators", *Technical Digest of the 1994 Solid-State Sensor and Actuator Workshop*, Hilton Head Isl., SC, June 1992, pp. 49-52.

HEXSIL TWEEZERS WITH PIEZORESISTIVE POLYSILICON STRAIN GAGES

Chris G. Keller[*] and Roger T. Howe[#]

Berkeley Sensor & Actuator Center
Depts. of [*]Materials Science and Mineral Engineering and [#]Electrical Engineering and Computer Sciences
University of California at Berkeley, Berkeley, California 94720-1774

ABSTRACT

High aspect ratio molded polysilicon (hexsil) tweezers with an integrated phosphorus doped thermal expansion actuator beam and piezoresistive polysilicon strain gages for tactile feedback are described. The tweezers are normally closed, and require 75 mW to open 50 μm. Piezoresistor performance remains to be measured. The tweezer tips and flexible electrical interconnects between rotating beams are surface micromachined polysilicon.

INTRODUCTION

Tweezers with integrated actuators and force sensors are essential for automated assembly of systems made up of independently microfabricated parts. The tweezers provide a mechanical interface between the macro and micro world: one end is macroscopic and can be coupled to conventional positioning actuators, while the other end is microscopic and can address small parts (e.g., 2 μm to 100 μm) with the appropriate forces of a few μNewtons.

The new features demonstrated here are (1) an integrated *in-situ* phosphorous doped polysilicon thermal expansion actuator that is maintained in tension (the previous design [1] operated in compression), (2) surface polysilicon flexures (Fig. 1) to support metal lines that carry signals from one rotating hexsil beam to the next, (3) surface polysilicon tips with piezoresistive boron implanted polysilicon resistors to measure gripping force (in-plane bending) and to detect contact with the table top (out-of-plane bending), (4) a full Wheatstone bridge on a semicircular flexure (Fig. 2) to sense tweezer tip position when no object is being gripped, (5) an efficient 4-bar linkage design with 30 to 1 leverage that amplifies the small motion of thermal expansion, (6) 100 μm long hexsil flexures at each pivot point to provide low in-plane stiffness.

THEORY

Fig. 3 shows the 8 mm long by 1.5 mm wide hexsil [1-3] tweezers in the open (power on) position. In use, the base of the tweezer is bonded to a 2 mm-wide, 5 cm-long bar that mounts into a 3-axis micrometer drive positioner on a probe station.

The thermal expansion element (light gray) is electrically isolated from the rest of the device. Current travels up one leg and down the other. The beam heats up and lengthens, causing the other beams in the two 4 bar linkages to rotate and open the tweezer tips. Thermal actuation has the advantages of simple fabrication and no sliding contacts which would be vulnerable to failure due to wear or contamination. The beam was made as long as possible (6 mm) to minimize the operating temperature for a given displacement.

The design stress in the hexsil flexures is compressive and less than 1 MPa, while the thermal expansion element is maintained under a tensile stress of less than 0.1 MPa. The yield stress of polysilicon exceeds 1 GPa, and it is expected that the structures will operate indefinitely.

Boron implanted polysilicon piezoresistors are used in a 1/4 bridge configuration at each tweezer tip, and a full Wheatstone bridge is fabricated on the semicircular flexure closest to the tips. The tip gages are located along one edge of the surface polysilicon
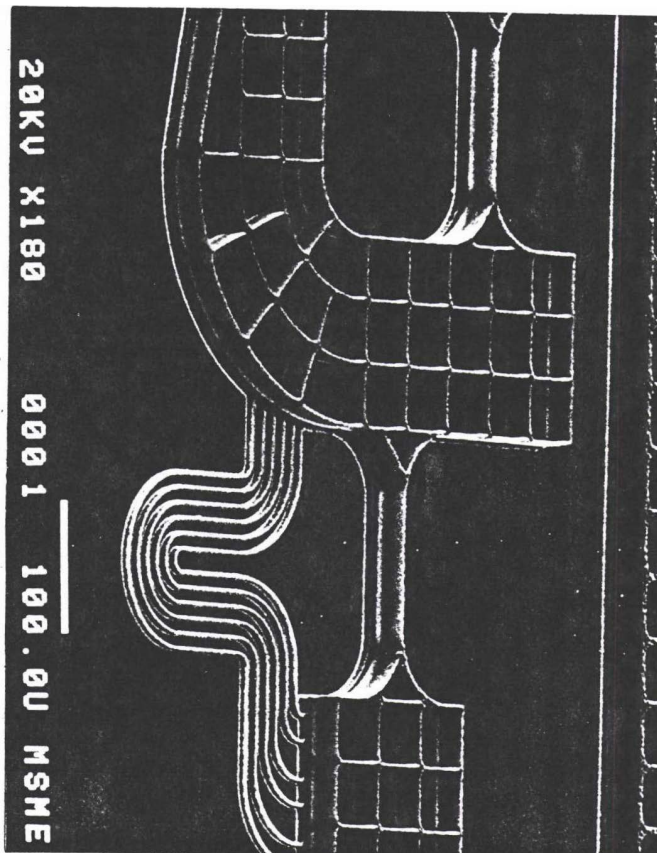

Figure 1. Surface poly flexures support metal lines between rotating hexsil beams; 100 μm long hexsil flexures allow in-plane rotation.
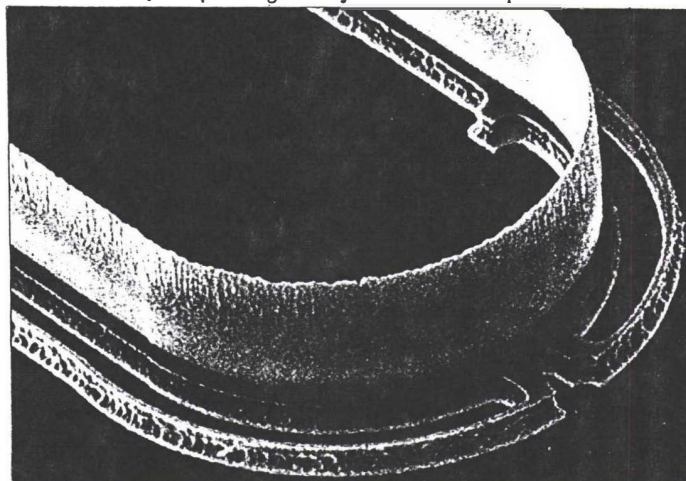

Figure 2. Bottom view of semicircular molded flexure with full Wheatstone bridge strain gage to sense tweezer tip position

beam (Fig.4) so that they are in tension when an object is being gripped. Compression in these gages indicates contact with an object in front of the tweezers. If they are being lowered, tension indicates contact with the table top. Figure 5 shows a side-view schematic of the stiffness transition from the 500 μm thick handle (B) to the 40 μm thick hexsil (H) to the 5 μm-thick surface polysilicon tips (S) to pick up an object (P). The tips are also shown in plan view. The set point for the closed position depends on the width of the object to be picked up. There should be just enough bending strain in the tips to hold the object against gravity, but not so much that they become unstable to out-of-plane bending (in which case one tip bends up, one bends down, and the object flips out of the grip, never to be seen again). To prevent this, power to the actuator would be servoed on the strain gage signal. Care should be taken to avoid electrostatic fields and sticky adsorbed organic films which over power gravity.

EXPERIMENTAL DETAILS

After the tweezers are released from the mold, the rigid base is picked up with ordinary hand held steel tweezers and put on a 1.5 mm x 0.5 mm x 0.02 mm spot of epoxy at the end of a 5 cm bar. A tungsten probe tip is used to pull the expansion beam 1 to 2 μm towards the base to close the tips, after which the beam is fixed to the base with a 100 μm diameter drop of epoxy. After the epoxy cures, the tungsten probe is removed. After assembly, all the slender flexures are in compression (but not enough to cause buckling) and the only tensile member is the actuator beam, which has a large cross sectional area so the tensile stress is low. Wires are epoxied to the 5 cm bar and positioned to contact the ends of the thermal expansion beam, and the 12 terminal pads for the strain gages. Electrical contact is made by applying a tiny drop of silver paint with a tungsten probe tip.

Although the tweezers are intended to operate with the thermal beam in tension, it is found that the 4 bar linkages are sufficiently compliant that the thermal beam can also operate in compression with out buckling. This allows the tips to be opened wider than their as-molded position.

Tip deflections of about 50 μm occur within less than 0.5 sec with 75 mW dissipated in the expansion beam. The body of the tweezer is 40 μm-high, 2-μm thick honeycomb cell walls (aspect ratio of 20:1). The strain gages are 0.4 μm thick and implanted with boron (5×10^{15}/ cm^2 at 30 keV).
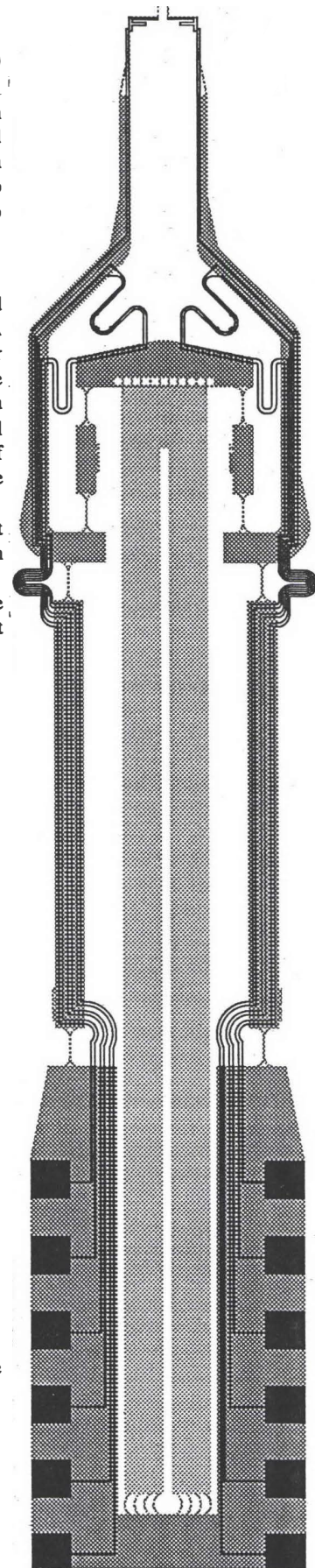

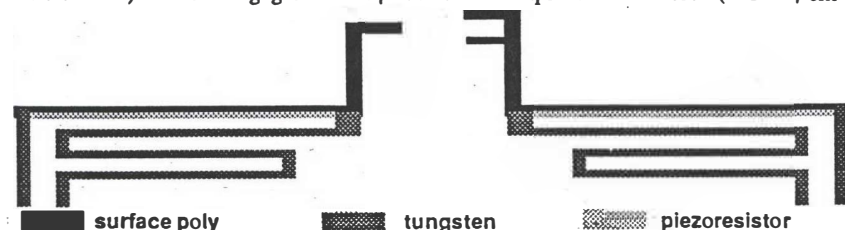**surface poly**   **tungsten**   **piezoresistor**

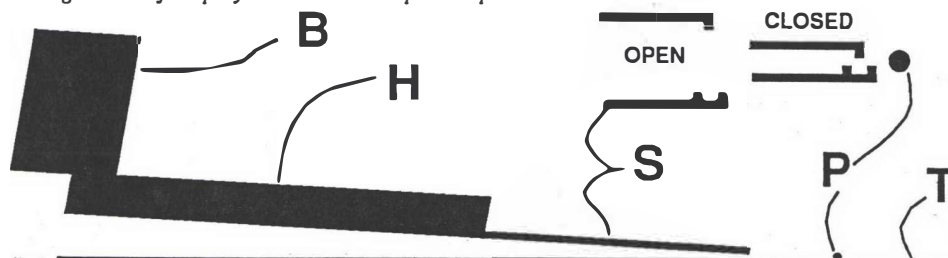*Figure 4 Surface polysilicon tweezer tips with piezoresistors*

Figure 5. Handle (B), hexsil (H), surface poly tweezer tips (S), table top (T), object to pick up (P)

CONCLUSIONS

Closed-loop operation of the tweezers remains to be demonstrated. Using molded polysilicon fabrication technology, a microactuator designer has access to a versatile tool set that will evolve into an infrastructure for the routine and convenient manipulation of microfabricated parts.

REFERENCES

1. C. G. Keller and R. T. Howe, "Nickel-Filled Hexsil Thermally Actuated Tweezers", Transducers 95, The 8th International Conference on Solid-State Sensors and Actuators, Stockholm, Sweden, June 1995, Vol. 2, pp. 376-379

2. C. G. Keller and R. T. Howe, "Hexsil Bimorphs for Vertical Actuation", Transducers 95, The 8th International Conference on Solid-State Sensors and Actuators, June 1995, Stockholm, Sweden, Vol. 1, pp. 99-102

3. C. G. Keller and M. Ferrari, "Milli-Scale Polysilicon Structures",1994 Solid State Sensor and Actuator Workshop, Hilton Head, S.C., June 1994, pp 132-137

Figure 3. Hexsil tweezers

HIGH-PRECISION SILICON MICROMACHINED MICROMIRRORS FOR LASER BEAM SCANNING AND POSITIONING

Meng-Hsiung Kiang, Olav Solgaard*, Richard S. Muller and Kam Y. Lau

Department of Electrical Engineering and Computer Sciences
University of California at Berkeley
Berkeley, CA 94720

*Department of Electrical and Computer Engineering
University of California at Davis
Davis, CA 95616

ABSTRACT

We present the design and fabrication of surface-micromachined micromirrors actuated by electrostatic-comb motors. High-precision positioning over a large angular range makes the micromirrors suitable for a variety of optical applications such as laser scanners and printers, displays, holographic-data storage, and fiber- optic switches.

INTRODUCTION

Silicon-surface-micromachining technology has been used to fabricate micro-optical devices such as movable-micromirrors for building optical components and communication subsystems [1-4]. Motorized micromirrors with actuators integrated on the same chip (such as those in [1-2]) are of particular interest because they make possible truly miniaturized systems. For practical optical systems, the smallest optical aperture (such as that of the mirror in our case) has to be large enough to insure sufficient image resolution. Polysilicon microhinges, which allow the micromirrors to be lifted out of the plane of the substrate after processing is completed, are used to create high-aspect-ratio optical surfaces with dimensions in the hundreds of μms while taking advantage of the planar surface-micromachining processing technology. Polysilicon torsion bars are used for mirror suspension in these structures and also for as the rotation shafts for the scanner.

We present here the design and fabrication of silicon-surface-micromachined scanning micromirrors that have high angular precision over a large scan angle. When used as resonant scanners, these mirrors have fast scan rates with very low operating power. We will discuss single-mirror scanners that are capable of high-speed scanning with a large scan angle. These single-mirror scanners can be combined to form more complicated microscanners such as a two-mirror, two-axis raster scanner that can have a wide range of applications in areas such as communications, medicine, and entertainment, among others.

ACTUATED MICROMIRROR DESIGN

The scanning micromirrors are fabricated using silicon-surface-micromachining processes [1,2]. Figure 1 shows SEM photographs of two comb-actuated micromirrors having orthogonal axes of rotation. The electrostatic comb drive for this scanner system consists of 100 interdigitated fingers for both the shuttle and the stationary comb on the two sides, with lateral dimensions totaling 1 mm. The motor is attached through a pair of restoring springs to a base plate that is hinged to the bottom of the micromirror. The double-folded restoring springs with truss suspensions have beams 2 μm wide and 300 μm long. The mirrors are mounted on the frames through two torsion bars (each 2 μm
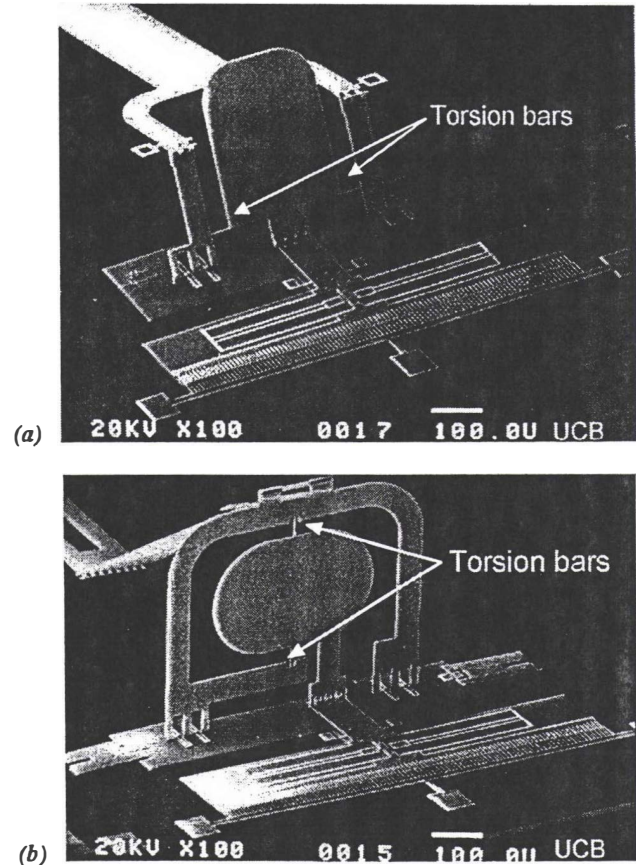

(a)

(b)

Fig. 1 SEM photographs of two electrostatic-comb-driven micromirrors having two different axes of rotation to enable scanning along two orthogonal axes. Both micromirrors measure 300 by 500 μm. a: θ (vertical)-scan mirror; b: φ (lateral)-scan mirror.

wide and 50 μm long) as the pivoting shafts for the mirrors. Two layers of structural polysilicon (each 2-μm thick) are used to complete the scanner structure. LPCVD silicon dioxide is used as the sacrificial material separating the different polysilicon layers.

CHARACTERIZATION

To characterize the performance of the scanning micromirrors, a position-sensing photodetector is used to record the position of a He-Ne laser beam reflected off the surface of the actuated micromirrors. The mirror in Fig. 1a is used first in our measurements. With varying dc-bias voltage (up- and down-ramp over many voltage cycles) to the electrostatic comb drive, the corresponding position of the reflected laser beam is plotted in

Fig. 2. The measurements show an angular position accuracy of 0.662 mrad in standard deviation. Over a total scan range of 0.1 rad, corresponds to 150 resolvable static-positions. On the other hand, if instead we drive the comb motor with an ac voltage close to or at its resonant frequency, the scanning laser beam scans in a smooth sinusoidal fashion over an excursion angle of 10°. It deviates from the sine-wave motion by 9.6 μm, or 0.19 mrad, in standard deviation along the scan line. This is a measure of the scan-line repeatability which is an important issue for optical scanning applications. Figure 3 is a measured result from the φ-scan mirror in Fig. 1b, showing also the sinusoidal motion over an excursion angle of 7°.
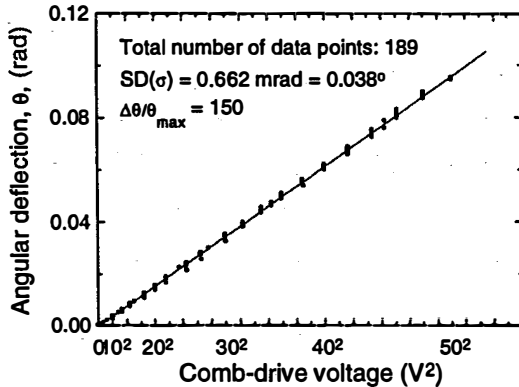
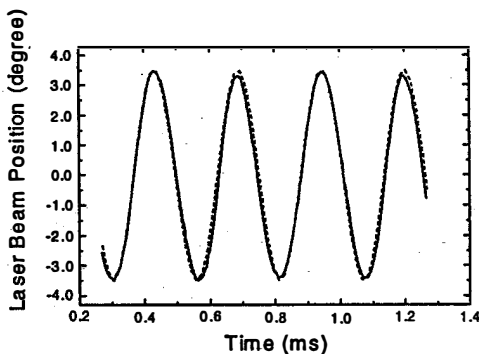Fig. 2 The static response of the θ-scanning micromirror to varying dc-bias voltage.

Fig. 3 Scanning laser beam (deflected by the mircroscanner shown in Fig. 1b) recorded with a position-sensing detector. The motor of the microscanner is driven by an ac voltage 30 V in amplitude at 2 kHz.

DISCUSSION

The use of torsion bar suspension provides accuracy in the control of the rotation angles. If we perform the same measurement as that for Fig. 2 with another scanning micromirror from our previous design [2] which uses micropin-hinges as the mirror shaft, the angular precision obtained (plotted in Fig. 4) is 3.3 mrad (compared with 0.662 mrad in Fig. 2). With a total scan angle of 0.21 rad, this corresponds to 63 resolvable static positions over the scan range. This reduction in angular accuracy can be attributed to the difference in the rotation-shaft structures for the two designs. As shown in the inset in Fig. 4, the armature of the micropin-hinge turns against a square shaft when the mirror rotates. As a result, the friction and drag cause a larger angular inaccuracy in mirror position. In addition, the wear in the shaft

structure in the micropin-hinge could potential be a concern for long-term reliability of the system.

The maximal scan angles in our present design, on the other hand, have been reduced from our previous case [2]. This is the result of using only two layers of polysilicon in the present structure that does not allow a mechanical design to compensate for the change in the elevation or the angle of the mirror base as the mirror rotates. Double-hinged base plate structure made of three layers of structural polysilicon (as that in [2]) will alleviate the problem and enable us to increase the scan range further.
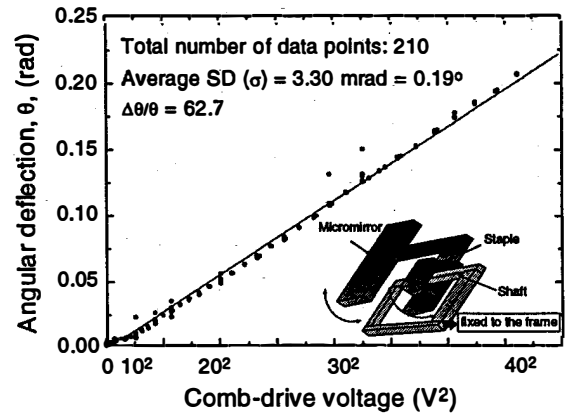

Fig. 4 The static responses of a θ-scan micromirror (described in [2]) to varying dc bias-voltage. The microscanner is a three-polysilicon structure with micropin-hinges as the rotation shafts.

CONCLUSION

We have designed and fabricated high precision polysilicon microscanners using surface micromachining. Electrostatic-comb actuators drive 300 by 500 μm micromirrors mounted on torsion bars. The microscanners are accurate to 0.662 mrad over 0.1 rad total scan range. In terms of static positioning, this corresponds to 150 resolvable positions, an almost three-fold improvement from structures using micropin-hinge design. This type of microscanner has previously been demonstrated as the scanner for a barcode reader [2]. Now, with higher angular precision, these electrostatic-comb-actuated micromirrors are also suitable for laser beam steering in more demanding optical scanning applications.

REFERENCES

[1] M.-H. Kiang, O. Solgaard, R. S. Muller, and K. Y. Lau, "Silicon-Micromachined Micromirrors with Integrated High-Precision Actuators for External Cavity Semiconductor Lasers," *IEEE Photon. Technol. Lett.,* Vol. 8, no. 1, pp. 95-97, 1996.

[2] M.-H. Kiang, O. Solgaard, R. S. Muller, and K. Y. Lau, "Surface-Micromachined Electrostatic-Comb Driven Scanning Micromirrors for Barcode Scanners," *Proceed. IEEE Micro Electro Mechanical Systems*, San Diego, CA, 2/12-16/96, pp. 175-180.

[3] O. Solgaard, M. Daneman, N. C. Tien, A. Friedberger, R. S. Muller, and K. Y. Lau, "Optoelectronic Packaging Using Silicon Surface-Micromachined Alignment Mirrors," *IEEE Photon. Technol. Lett.*, Vol. 7, no. 1, pp. 41-43, 1995.

[4] Y. Lin, S. S. Lee, K. S. Pister, and M. C. Wu, "Micro-machined Three-dimensional Micro-optics for Integrated Free-space Optical Systems," *IEEE Photon. Technol. Lett.*, Vol. 6, no. 12, pp. 1445-1447, 1994.

3.5 Mbit/sec. MARS Modulator System Performance for Fiber-to-the-Home Applications

J.A. Walker[1], K.W. Goossen[1], P.P. Iannone[2], W.M. MacDonald[3], R. Ruel[3], R. Boie[4], S.C. Arney[3], N.J. Frigo[2], and D.J. Bishop[3]

[1]Bell Laboratories, Lucent Technologies, 101 Crawfords Corner Rd., Rm 4B-511, Holmdel, NJ 07733
[2]Bell Laboratories, Lucent Technologies, Murray Hill, NJ
[3]AT&T Research, Holmdel, NJ
[4]AT&T Research, Murray Hill, NJ

INTRODUCTION

Wavelength Division Multiplexed Passive Optical Network Systems (WDM-PONS) show promise of providing a cost-effective method of obtaining fiber-to-the-home telecommunications networks. The Mechanical Anti-Reflection Switch (MARS) optical modulator has been developed for use as a moderate datarate (a few Mbit/sec.) component for a class of WDM-PONS systems utilizing "loop-back" principles [1]. Loop-back refers to systems which utilize a modulator at the subscriber node to overmodulate light sent downstream from the central office to the user and loop it back upstream to the central office. An important advantage of this type of WDM system is the ability to cost share high performance sources and detectors at the central office while utilizing unshared, low cost, moderate performance components at the subscriber node.
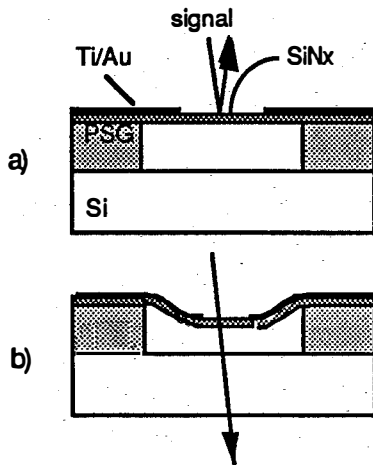

Figure 1: *MARS modulation principle.*

A difficulty arises from the fact that these low cost components must still meet some rather challenging requirements, moderate data rate (>1 Mbit/sec.), wide spectral width in order to provide many wavelength channels, high contrast ratio (>10 dB modulation depth), and good thermal stability. The MARS modulator has been demonstrated to meet or surpass all of these requirements as well as allow extremely inexpensive optical packaging techniques to be used in order to reduce the cost of the fully packaged device. The performance and packaging cost implications of the MARS device are discussed here.

MARS DEVICE PRINCIPLE

The MARS device is an optical modulator based on the principle of a vertically moving anti-reflection film suspended above a silicon substrate [2]. The operating principle and device structure are shown in Fig. 1. Anti-reflection films are well known in the optics community, and are formed by depositing a dielectric film upon the surface desired to be anti-reflective. The dielectric film is required to have a

refractive index equal to $\sqrt{n_s}$ (where n_s is the refractive index of the substrate) and a thickness equal to $\lambda_o/4$ where λ_o is the center wavelength of the incident light spectrum. If this anti-reflection film is suspended above the substrate by an air gap equal to $\lambda_o/4$, instead of an anti-reflecting condition, a highly reflecting condition is then achieved. This reflecting/anti-reflecting condition holds for all air gaps equal to $m\lambda_o/4$, reflecting if m is odd, anti-reflecting if m is even. As m increases however, the spectral width of the device narrows, reducing the number of wavelength channels for which a modulator could operate. The operating principles of the MARS device are discussed more thoroughly in Reference 2, and the fabrication is discussed in Reference 3.
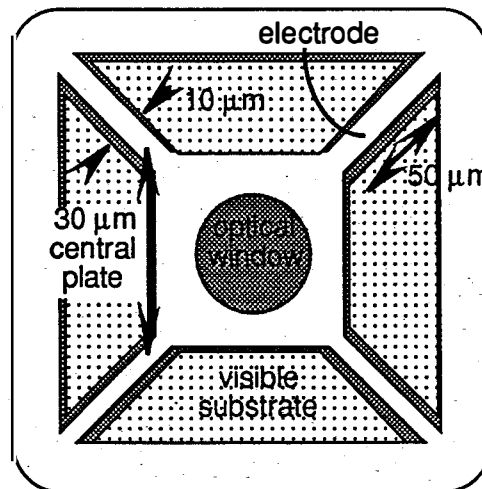

Figure 2: *Top view of a MARS design.*

A typical device geometry is shown in Fig. 2. The MARS consists of a central plate suspended above the substrate via support beams, comprising the mechanically active area of the device. An optical window is defined by the absence of electrode material in the center of the plate area. Modulators

with central plates ranging from 10 μm x 10 μm to 100 μm x 100 μm, support beams ranging from 4 μm wide to 21 μm wide, and 5 μm long to 100 μm long have been fabricated and tested.

SYSTEM PERFORMANCE

Typically rise and fall times of roughly 130 ns are measured for standard modulators. With some device geometries, the response includes mechanical ringing at characteristic resonant frequencies of up to 4 MHz. With straight forward device design changes, this ringing can be reduced and modeling predicts that usable data rates can be achieved at three times the resonant frequency of a device, or up to 12 Mbit/sec. In practice however, we have yet to demonstrate system operation at such high data rates. System experiments have been run to determine bit-error-rates for fully packaged devices under normal operating conditions. The measurement apparatus used for system tests is shown in Figure 3. Figure 4 shows the response of such a modulator to a pseudo random bit stream of 2^{15}-1 word length at 3.5 Mbit/sec.
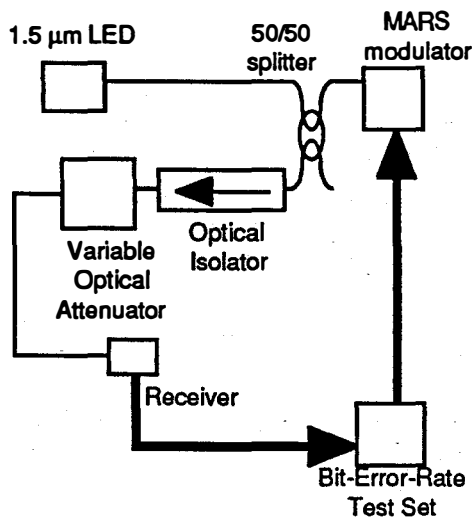
Figure 3: *Bit-error-rate measurement apparatus.*

As shown in Fig. 4, the modulator can achieve this data rate with error rates of less than 10^{-8} with less than 2 dB power penalty from the system base band. This penalty arises mainly from pattern dependent inter-symbol interference.

PACKAGING CONSIDERATIONS

The final cost of a packaged MARS modulator will be dominated by the expense of the packaging process, particularly optical fiber attachment. Here, the MARS modulator has some distinct advantages. Due to the large optical window (20-30 μm), inherent polarization insensitivity, and uncomplicated fabrication, multi-mode packaging techniques can be exploited to obtain single-mode fiber devices. Measurements show an alignment tolerance an order of magnitude larger than typical single mode devices, large enough to enable passive packaging

techniques. This would eliminate the expensive active alignment process used for most photonic packages today, greatly reducing cost.
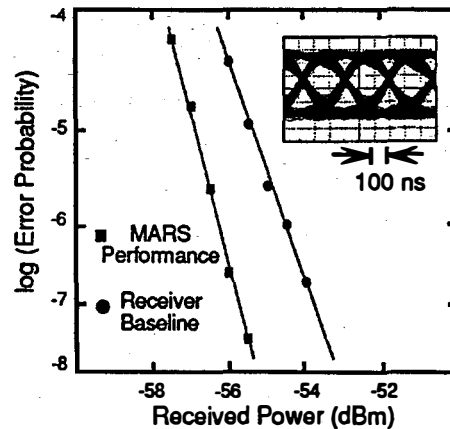

Figure 4: BER result and eye pattern for a fully packaged modulator.

CONCLUSION

We have demonstrated a micromechanical modulator with the capability of providing upstream data rates of 3.5 Mbit/sec with 10^{-8} BER in a fiber-to-the-home communications system. Due to several advantageous aspects of the MARS, packaging costs for the device should be quite low, resulting in an extremely inexpensive moderate data rate optical modulator.

REFERENCES

[1] N.J. Frigo, P.P. Iannone, P.D. Magill, T.E. Darcie, M.M. Downs, B.N. Desai, U.Koren, T.L. Koch, C. Dragone, H.M. Presby, and B.E. Bodeep, "A wavelength-division multiplexed passive optical network with cost-shared components," *IEEE Phot. Tech. Lett.*, vol. 6, pp. 1365-1367, (1994).

[2] K.W. Goossen, J.A. Walker, and S.C. Arney, "Silicon modulator based on mechanically-active anti-reflection layer with 1 Mbit/sec. capability for fiber-in-the-loop applications," *IEEE Phot. Tech. Lett.*, vol. 6, pp. 1119-1121, (1994).

[3] J.A. Walker, K.W. Goossen, and S.C. Arney, "Fabrication of a mechanical anti-reflection switch for fiber to the home systems," *J. Micromech. Syst.*, vol. 5, no. 1, pp. 45-51, (1996).

AUTHOR INDEX